AGU PUBLICATIONS

JGR

Journal of Geophysical Research: Atmospheres

RESEARCH ARTICLE
10.1002/2017JD027331

Key Points:
- An end-to-end simulation sequence provides black carbon estimates for evaluating climate impacts of a nuclear exchange
- Detailed fire simulations reveal that black carbon particles reside primarily in the troposphere
- Climate impacts of a nuclear exchange are significantly diminished by precipitation scavenging of tropospheric particles

Correspondence to:
J. Reisner,
reisner@lanl.gov

Citation:
Reisner, J., D'Angelo, G., Koo, E., Even, W., Hecht, M., Hunke, E., et al. (2018). Climate impact of a regional nuclear weapons exchange: An improved assessment based on detailed source calculations. *Journal of Geophysical Research: Atmospheres*, *123*, 2752–2772. https://doi.org/10.1002/2017JD027331

Received 20 JUN 2017
Accepted 1 FEB 2018
Accepted article online 13 FEB 2018
Published online 14 MAR 2018

Climate Impact of a Regional Nuclear Weapons Exchange: An Improved Assessment Based On Detailed Source Calculations

Jon Reisner[1], Gennaro D'Angelo[1], Eunmo Koo[1], Wesley Even[1], Matthew Hecht[1], Elizabeth Hunke[1], Darin Comeau[1], Randall Bos[1], and James Cooley[1]

[1]Los Alamos National Laboratory, Los Alamos, NM, USA

Abstract We present a multiscale study examining the impact of a regional exchange of nuclear weapons on global climate. Our models investigate multiple phases of the effects of nuclear weapons usage, including growth and rise of the nuclear fireball, ignition and spread of the induced firestorm, and comprehensive Earth system modeling of the oceans, land, ice, and atmosphere. This study follows from the scenario originally envisioned by Robock, Oman, Stenchikov, et al. (2007, https://doi.org/10.5194/acp-7-2003-2007), based on the analysis of Toon et al. (2007, https://doi.org/10.5194/acp-7-1973-2007), which assumes a regional exchange between India and Pakistan of fifty 15 kt weapons detonated by each side. We expand this scenario by modeling the processes that lead to production of black carbon, in order to refine the black carbon forcing estimates of these previous studies. When the Earth system model is initiated with 5×10^9 kg of black carbon in the upper troposphere (approximately from 9 to 13 km), the impact on climate variables such as global temperature and precipitation in our simulations is similar to that predicted by previously published work. However, while our thorough simulations of the firestorm produce about 3.7×10^9 kg of black carbon, we find that the vast majority of the black carbon never reaches an altitude above weather systems (approximately 12 km). Therefore, our Earth system model simulations conducted with model-informed atmospheric distributions of black carbon produce significantly lower global climatic impacts than assessed in prior studies, as the carbon at lower altitudes is more quickly removed from the atmosphere. In addition, our model ensembles indicate that statistically significant effects on global surface temperatures are limited to the first 5 years and are much smaller in magnitude than those shown in earlier works. None of the simulations produced a nuclear winter effect. We find that the effects on global surface temperatures are not uniform and are concentrated primarily around the highest arctic latitudes, dramatically reducing the global impact on human health and agriculture compared with that reported by earlier studies. Our analysis demonstrates that the probability of significant global cooling from a limited exchange scenario as envisioned in previous studies is highly unlikely, a conclusion supported by examination of natural analogs, such as large forest fires and volcanic eruptions.

1. Introduction

Beginning in the early 1980s, high-profile journal articles (e.g., Crutzen & Birks, 1982; Pittock et al., 1986; Turco et al., 1983) that highlighted the impact of nuclear weapons on human population via a variety of effects such as blasts, fallouts, and fires began appearing. The last effect, by its ability to produce small black carbon (BC) particles or soot via combustion of various materials found within an urban environment and subsequent blocking of incoming solar radiation, became broadly known as "nuclear winter" in the literature. While blast and fallout impacts are typically localized near the detonation, especially for weapon yields significantly below a megaton and for ground bursts, nuclear winter is a global phenomenon and may induce subfreezing temperatures over a decadal time period. In fact, fear from this perceived threat was one reason for the significant reductions in nuclear weapon stockpiles in the former Soviet Union and the United States during the later 1980s (Robock, 1989).

Although the threat of a large-scale nuclear exchange between the superpowers has diminished significantly, the possibility of a more limited exchange between countries such as India and Pakistan also must be considered. A recent series of papers (e.g., Mills et al., 2014; Robock, Oman, Stenchikov, et al., 2007; Robock, Oman, & Stenchikov, 2007; Robock & Toon, 2010; Toon et al., 2007, 2008) suggested that even a limited nuclear exchange between India and Pakistan would lead to a significant loss of life on the order of a billion

people due to significant global cooling induced by burning buildings and vegetation. The authors' explanation of how a regional exchange of small-yield nuclear weapons could induce significant global cooling is based upon the assumption that BC particles produced by burning buildings and vegetation are small and are readily transported into the upper atmosphere via fire-induced plume dynamics. Further, once deposited in the lower stratosphere, the authors argue that these BC particles absorb significant solar energy, heating the surrounding gas and inducing significant upward and outward transport of a majority of the BC particles into the upper stratosphere. There they would block incoming solar radiation over a large, possibly global, region, leading to potentially significant cooling. In this paper, we aim to show that by combining results from comprehensive models of fire and weapons effects with a state-of-the-art Earth system model, we are able to provide more accurate estimates of the resulting BC forcing on climate and a revised assessment of potential global climatic impacts of a limited nuclear exchange.

A necessary condition for significant global cooling impacts from a limited exchange is that the atmosphere and fuel be conducive to fire and subsequent upward transport of BC. Unlike a volcano with superheated buoyantly driven exhaust material from the caldera moving rapidly upward and being rapidly transported into the stratosphere (Ogden, Wohletz, et al., 2008; Ogden, Glatzmaier, & Wohletz, 2008), environmental conditions can inhibit BC transport in nuclear exchange events. For example, if the exchange takes place during the winter, or when clouds are present, or if the winds are too high or too light to prevent fire spread, and/or if it is raining or has recently rained, the amount of BC produced and/or the amount that reaches the lower stratosphere could be relatively small. Likewise, if remote military sites are primarily targeted instead of cities, the amount of BC produced will also be substantially reduced. The impacts of the detailed selections of both geography and meteorology for the scenario could significantly decrease the likelihood of a significant global cooling. Our analysis evaluates the likelihood of significant global variations of climate variables, such as surface temperature and precipitation, associated with a limited nuclear exchange.

The U.S. Department of Energy/National Nuclear Security Administration national laboratories are well positioned to contribute to an understanding of the conditions under which significant global cooling or even nuclear winter may occur from a nuclear exchange. For the present study, we draw upon a knowledge base that includes expertise in the science and modeling of rubblization of buildings, fireball evolution from initial source to subsequent fallout, and climate-related fire impact. In particular, we explore various factors that could induce nuclear winter effects, including computation of the amount of debris lofted by the fireball, burning and transport of BC from a representative city, and utilization of the calculated BC profile in climate simulation ensembles to assess its impact on global-scale cooling. Further, while this study is motivated by an exchange between India and Pakistan, the overall modeling system described in this paper could be used to assess possible exchanges involving other countries and weapon configurations. In the next section, we describe the various models and how they were used in a worst case scenario to assess a possible nuclear winter outcome. In the remaining sections, key results from the various models will be presented, with a final summary of conclusions from our end-to-end modeling study.

2. Model Descriptions

We utilize several Los Alamos National Laboratory numerical models that have an established history of nuclear effects simulation: xRage and Cassio, a fireball modeling system, and HIGRAD-FIRETEC, a fire model. In additional to these key models, we also use the Community Earth System Model (CESM), maintained at the National Center for Atmospheric Research (NCAR), to study various nuclear winter scenarios. Each component model's configuration is designed to represent a limited nuclear exchange as originally postulated by Robock, Oman, Stenchikov, et al. (2007), involving 100 low-yield weapons of 15 kilotons (kt) each (50 from each side), dispersed over various cities within India and Pakistan. The climatic impacts of this scenario, which is based on the extensive analysis of Toon et al. (2007), were also assessed by means of CESM in Mills et al. (2008, 2014).

2.1. Fireball Modeling System: xRage

xRage (Gittings et al., 2008) is a radiation hydrodynamics code that solves the Euler equations for hydrodynamics fully coupled with a diffusion equation for radiation transport on an adaptive mesh. xRAGE supports multiple material formulations and material strength and damage; hence, xRage can be used to examine the formation of dust and debris materials by a fireball upon impact with the ground and their entrainment into the flow. The code has undergone rigorous testing, and xRage has been used to model a wide variety of

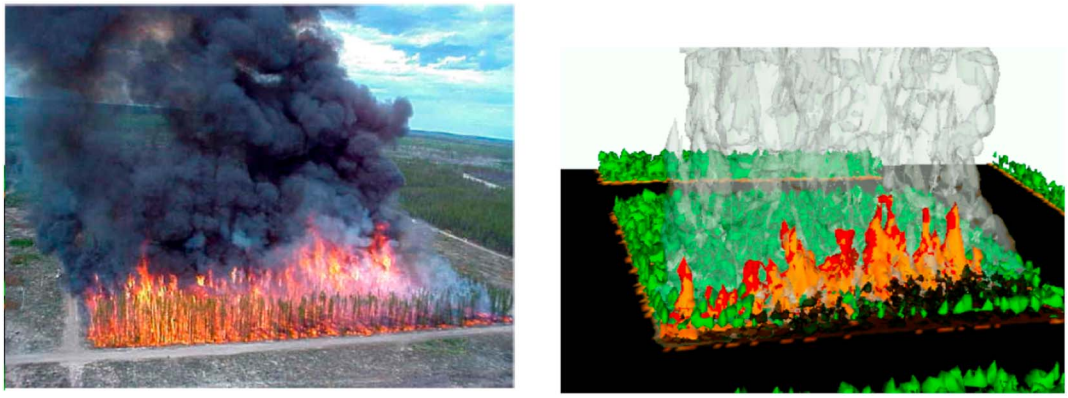

Figure 1. (left) Image of a controlled burn from a Canadian experiment (see Pimont et al., 2009 for a discussion of this experiment). (right) A HIGRAD-FIRETEC simulation of the controlled burn.

applications including astrophysics (Frey et al., 2013), high-energy density physics (Doss et al., 2013), inertial confinement fusion (Bradley et al., 2012), and impact cratering (Korycansky et al., 2009). The purpose of the xRage simulation was to illustrate that the amount of material produced by the shock interacting with the ground and subsequent pickup of material is many orders of magnitude smaller than the amount of BC produced by the fires. Note that this may not be the case for larger weapon yields using surface bursts.

The specific scenario that is simulated is a 15 kt blast originating within an initial radius of 40 cm at an initial height of 50 m. The density and temperature of the atmosphere are derived from the 1976 U.S. Standard Atmosphere, and the ground is composed of Nevada tuff, for comparison against above-ground test data. The simulation is initiated by sourcing 15 kt of energy uniformly into the source region over 40 ns. The two-dimensional xRage mesh spans 6.5 km in the horizontal direction and 4 km in the vertical direction. Adaptive mesh refinement is active with the highest refinement being 2 cm near the fireball and decreasing to 50 cm away from these regions. The simulation was run to 3.5 min to stabilize the fireball and debris altitude.

2.2. Fire Modeling System: HIGRAD-FIRETEC

The HIGRAD model (Fierro & Reisner, 2010; Margolin & Reisner, 2016; Reisner & Jeffery, 2009) solves the compressible Navier-Stokes equations, and when linked to various physics packages such as FIRETEC, a physics-based fire dynamics model (Canfield et al., 2014; Linn, 1997; Linn et al., 2005, 2010; Linn & Cunningham, 2005; Pimont et al., 2016), HIGRAD-FIRETEC can be used to study the evolution and spread of fire and its two-way interaction with atmospheric dynamics. The HIGRAD-FIRETEC modeling system has been used to simulate a wide variety of fire behavior over the past 20 years, from slow-moving grass fires to fast-moving mass fires in an urban environment. A key aspect of this work involves validation of the model against observed fires, both natural and controlled (Linn, Anderson, et al., 2012; Linn, Canfield, et al., 2012; Pimont et al., 2009; see Figure 1). Thus, this modeling tool is uniquely able to address the formation and transport of BC produced by large urban fires and provide realistic emission profiles to a climate model for addressing possible nuclear winter-related concerns.

In the context of this paper, HIGRAD-FIRETEC is used to examine mass fires resulting from the detonation of small nuclear devices over a city landscape. A mass fire starts from many simultaneous ignition points (100,000 or more in our model) produced from the thermal radiation of a nuclear weapon that can quickly combine into a large fire with significant updrafts and high-velocity indrafts. But, due to the indrafts, outward fire spread is small in low ambient wind conditions, and unless significant secondary ignitions take place, a mass fire can quickly burn itself out within an hour or two. Further, in this paper, the impact of secondary ignitions, such as gas line breaks, is not considered and research is still needed to determine their impact on a mass fire's intensity. For example, evidence of secondary ignitions in the Hiroshima conflagration ensuing the nuclear bombing (National Research Council, 1985), or utilization of incendiary bombs in Dresden and Hamburg (Hewitt, 1983), led to unique conditions that resulted in significantly enhanced fire behavior.

Here we provide a complete description of the setup used in HIGRAD-FIRETEC simulations of urban fire scenarios after the detonation of a 15 kt device. As indicated below, the simulations include various worst case

assumptions with regard to the specification of the fuel, weather conditions, and height of burst of the device. Therefore, they serve as upper bounds with regard to the expected outcome of an urban mass fire caused by a nuclear detonation. As for fuel conditions, the worst case "no-rubble" scenario is compared with the more realistic "rubble" scenario, in which building damage by the detonation affects ignition probability and fuel availability. At the opposite end, the "no-rubble" case assumes that all the buildings remain intact and all combustible materials in the buildings are available for ignition and fire spread. For the vertical transport of the BC, very calm ambient winds are assumed in the model, so to prevent rapid dispersion of the BC in the plume. The height of burst is determined as twice the fallout-free height, so to minimize building damage and to maximize the number of ignited locations. Fire propagation in the model occurs primarily via convective heat transfer and spotting ignition due to firebrands, and the spotting ignition model employs relatively high ignition probabilities as another worst case condition. Further, because the current version of FIRETEC assumes BC production to be inversely proportional to oxygen depletion (no soot model was employed), that is, all the carbon in the fuel participated in the reaction and was turned into BC, the estimates, which represent upper bounds for the given fuel loadings, are higher (worst case) than they would be if a detailed chemical combustion model was used for soot production. Although FIRETEC does not presently include this capability, it does have the ability to simulate combustion of fuel and fire spread though heat transfer, while other fire-modeling tools, such as WRF-FIRE (Coen et al., 2013), employ prescribed fire spread approximations typically based on wind speed and direction.

After potential sites in the India-Pakistan region were examined using Google Earth, both building and vegetation data, to be modeled as fuel in HIGRAD-FIRETEC, from a section of suburban Atlanta, GA, were chosen for use as a "generic suburb" for the study. Of note is that FIRETEC does not represent the burning of entire buildings if they are not composed of wood, but it does burn the both thermally thin and thermally thick combustible material that is found in the buildings, for example, paper (thermally thin) and wooden furniture (thermally thick) in offices. Hence, information is needed with regard to defining this important fuel quantity, which is typically only known for a few select U.S. cities. Likewise, examination of cities in India and Pakistan suggests the construction to be primarily concrete, as opposed to wood in suburban Atlanta. Hence, while the building density may be lower than cities in India or Pakistan, the buildings in Atlanta will burn at higher intensity due to contributions from both thick and thin fuels. Building and vegetation data for Atlanta were imported from NucFast, a fast-running tool for weapon effects developed by Applied Research Associates, Inc. NucFast includes Geographical Information System (GIS) data for major U.S. cities and also imports vegetation data from the LANDFIRE database (https://www.landfire.gov/); thus, if needed, this software could be used to examine urban firestorms for other U.S. locations.

Given the small 15 kt yield, a 10 km by 10 km area for ground effects was specified in NucFast. The burst height was set as 324.16 m (twice the fallout-free height of the burst) and defines the rubblization zone (the area where buildings are destroyed by the blast wave and are thus not available as fuel) produced by NucFast. Vegetation fuel, which is more flexible than building fuel, is assumed not to be rubblized by the burst. The simulations are performed for both fuel setups, that is, the "no-rubble" case, which assumes that the buildings are not damaged and all the combustible materials in the buildings remain intact and available for ignition (worst case), and the "rubble" case, which uses NucFast calculations of building damage, so that the whole or portions of the damaged buildings are turned into rubble piles. Because of lack of oxygen supply, it is assumed that the combustibles in the rubble piles are unavailable for ignition and fire spread.

The ignition map is also obtained from a NucFast run and provides probabilities of ignition for the various fuel types. Vegetation is modeled as thermally thin fuels with various moisture contents, while thin fuels in buildings (paper) are modeled with 2% moisture content, which can be considered to be "dry". The fuel loadings for vegetation are estimated from the LANDFIRE database, which utilizes Anderson fuel types (Anderson, 1982) for surface fuels and canopy bulk density and heights for canopy fuels. The LANDFIRE database and Anderson fuel types are built primarily for wildfire spread models; thus, they only account for thermally thin fuels. In many wildfire scenarios, thick vegetation material, such as tree trunks, contributes little to fire spread, by smoldering on the outer surface or not burning at all, because of high moisture contents of live vegetation. But in firestorms or in extreme events of large-scale fires, thick vegetation can contribute to fire behavior and BC injection to the atmosphere. For the current urban scenario, this effect is assumed to be small for the thick vegetation fuels.

Table 1
Fuel Loading for Different Building Types

Hazus building type	Description	Total fuel density (kg m^{-3})	Thin fuel density (kg m^{-3})	Thick fuel density (kg m^{-3})	Thin fuel fraction	Fuel loading with average building height[a] (kg m^{-2})
1	Attached commercial (office, retail, etc.) (brick)	8.330	1.250	7.081	0.150	88.673
2	Attached commercial (office, retail, etc.) (frame)	8.330	1.250	7.081	0.150	88.673
3	Detached close set commercial offices	8.330	1.250	7.081	0.150	88.673
4	Detached close set residential house/apartments	10.833	1.625	9.208	0.150	115.317
5	Detached close set houses	10.833	1.625	9.208	0.150	115.317
6	Single-story detached close set industrial storage	16.380	1.229	15.152	0.075	174.365
7	Religious	8.330	1.250	7.081	0.150	88.673
8	Monumental (political, commercial)	5.830	0.875	4.956	0.150	62.060
9	Residential wooden house	12.000	2.400	9.600	0.200	127.740
10	Mobile home	12.000	2.400	9.600	0.200	127.740

[a]Average building height in the selected site is 10.645 m.

Within FIRETEC, buildings are modeled as thermally thick and thin fuels with less moisture than vegetation fuel, with the various buildings having different combustible material loads and percentages of these two fuel types (Bukowski, 2006) from the Hazus database (http://www.fema.gov/hazus). Table 1 shows building types in the Hazus database and estimated fuel loading per volume, based on data from Bukowski (2006) of total fuel loading per area per one-story data. In order to convert the fuel loading data to per volume for use in FIRETEC, estimated building heights for different occupancy types (e.g., commercial versus suburban residential) were used. Fractions of thin fuel and thick fuel for use in FIRETEC were also estimated for different building types, as shown in Table 1.

In HIGRAD-FIRETEC simulations, NucFast ignition probabilities of thin and thick fuels are taken as input parameters, and solid fuel temperatures are heated to target ignition temperatures for the ignited fuel. Once the solid temperatures reach the targets, the combustion model in FIRETEC controls the fuel consumption due to chemical reaction and the transfer of heat to the gas, resulting in a grid cell whose contents are essentially on fire. Target average temperatures and ramping rates are set differently for thin fuel and thick fuels; for thin fuel, the target average ignition temperature is 1000 K, ramping at 350 K/s, thus taking 2 s to reach 1000 K when starting from 300 K. For thick fuel, the target average ignition temperature is 600 K, ramping at 210 K/s, taking 1.43 s to reach 600 K when starting from 300 K. Since the reaction of solid fuels in FIRETEC grid cells is represented by the average temperature and probability density functions, lower average temperature of thermally thick fuel means that a less fraction of thick fuels in the grid cells is burning than thin fuels, not that the actual flame temperature is lower for thick fuels. Likewise, lower ramping rate means slower fire spread over thick fuels within a FIRETEC grid cell. After the target average temperature is reached in the ignition stage, the reaction model controls the fuel temperature, which can reach above 2000 K in grid cells containing active burning. Heat and oxygen transfer within adjacent cells are calculated in FIRETEC, so when a cell is on fire, the fire can spread to adjacent cells, or can be extinguished if it loses too much heat to adjacent cells or not enough oxygen is supplied from adjacent cells. The "rubble" and "no-rubble" scenarios show different fire behavior because different conditions result in different balances in heat, oxygen transfer, and combustion within FIRETEC cells.

Indeed, Figure 2 reveals the initial fire starts over the simulation domains and illustrates the large areal extent of the initial mass fires with the no-rubble simulation clearly having more fire starts. In particular, the no-rubble simulation has over 400,000 grid points that are initially ignited, whereas the rubble simulation only contains approximately 30,000 initially ignited grid points. As will be seen in the results section, this large difference in initial fire intensity translates into a more intense mass fire that transports more BC into the upper atmosphere than does the simulation containing rubble.

Figure 3 shows the initial vertical profiles of wind speed and potential temperature used for the HIGRAD-FIRETEC simulations. The wind speed profile was chosen to be high enough to maintain fire spread but low enough to keep the plume from tilting too much to prevent significant plume rise (worst case). Wind direction is set as 270° (west-to-east, $+x$ direction) for all heights, with no directional shear, and a weakly

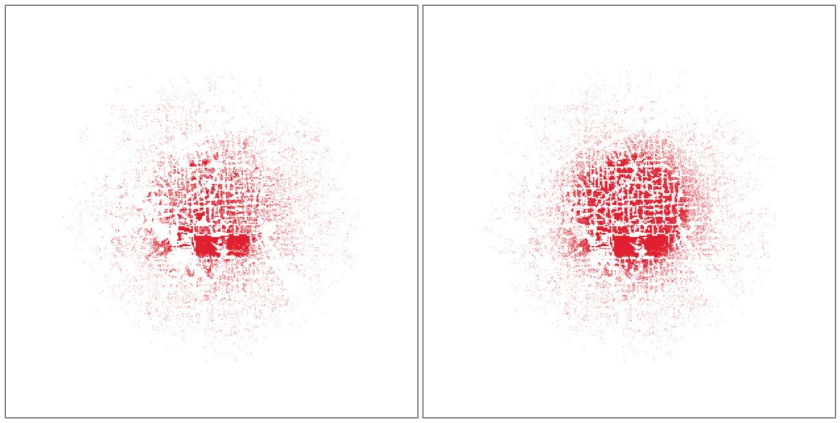

Figure 2. Initial fire starts (indicated by red shading) from a simulation containing rubble (left) and from no rubble (right) in a 10 km by 10 km area.

stable atmosphere was used below the tropopause to assist plume rise (worst case). In the future, linkage to xRage will be undertaken to better define the initial state after a nuclear detonation; for example, the assumption of a quiescent initial state should be investigated with regard to its impact on plume rise and injection of carbon into the upper atmosphere. A dry atmosphere was utilized, and pyrocumulus impacts or precipitation from pyrocumulonimbus were not considered. While latent heat released by condensation could lead to enhanced vertical motions of the air, increased scavenging of soot particles by precipitation is also possible (e.g., the black rains noted in both Hiroshima and Nagasaki, Pittock et al., 1986; Sakata et al., 2014). These processes will be examined in future studies using HIGRAD-FIRETEC.

Though the wind speed was relatively light, a larger computational domain, 20 km × 10 km × 18 km, was used for the simulations to help ensure that the BC remained within the computational domain over the 40 min integration time period. Note that because of low wind speeds and hence minimal fire spread, the fires are rapidly subsiding at 40 min (not shown). For this domain, 2,000 × 1,000 × 300 computational grid cells were used with vertical stretching. The horizontal resolution is 10 m with varying cell heights, from 12 m at the bottom to 155 m at 18 km. HIGRAD-FIRETEC simulations for this domain used 5,000 processors and took roughly 96 h to complete for 40 min of simulated time.

2.3. Global Climate Model: CESM

The impact on global climate of BC aerosol produced by combustion within the HIGRAD-FIRETEC model was studied with CESM, a global Earth system model in which land, ocean, sea ice, and atmospheric components are fully coupled. This comprehensive model provides state-of-the-art simulations of the Earth's past, present, and future climate (Gent et al., 2011; Hurrell et al., 2013; Neale et al., 2010). The experiments reported herein are based on the CESM 1.2 series, 2014 release (1.2.2).

The atmospheric component uses the Whole Atmosphere Community Climate Model (WACCM) version 4 (Marsh et al., 2013; Mills et al., 2014), which is an extension of the Community Atmospheric Model version 4

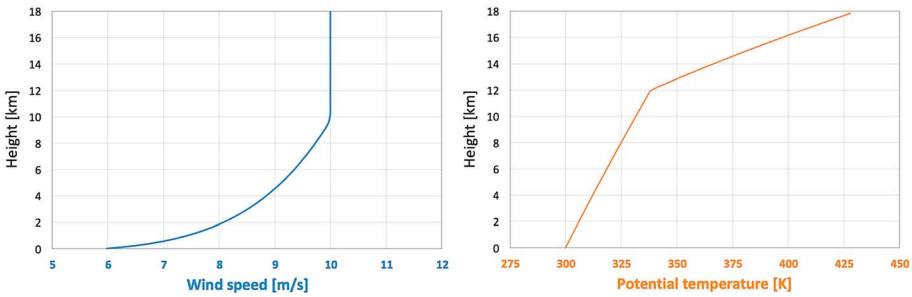

Figure 3. Initial vertical profiles of wind speed and potential temperature used in the HIGRAD-FIRETEC simulations.

(Neale et al., 2013). WACCM is a chemistry climate model with resolved stratosphere and mesosphere and extending in the thermosphere up to a height that corresponds to a pressure of about 5×10^{-6} hPa (approximately 140 km). The model has a 1.9° latitude × 2.5° longitude horizontal resolution and 66 vertical levels. The land component uses the Community Land Model version 4 (Lawrence et al., 2011; Oleson et al., 2010), on the horizontal grid of the atmospheric model. The ocean component is a level-coordinate model based on the Parallel Ocean Program of the Los Alamos National Laboratory, version 2 (Danabasoglu et al., 2012; Smith et al., 2010). The ocean model applies a 1° × 1° horizontal resolution and has 60 vertical levels, down to a depth of 5,500 m. The sea ice component is the Los Alamos National Laboratory sea ice model version 4 (Holland et al., 2012; Hunke & Lipscomb, 2008), and uses the ocean model horizontal grid. In the simulations, these components are all active; that is, the model is fully prognostic.

The atmospheric component of CESM was configured to use the Community Aerosol and Radiation Model for Atmospheres version 3 (for further details, see Mills et al., 2014, and references therein). This package, specifically designed for the microphysical treatment of atmospheric particulates, was adapted to model the dynamical and radiative interactions of BC aerosol with the atmosphere. The Community Aerosol and Radiation Model can simulate the evolution of a size distribution of particles, including growth by coagulation and condensation. This study, however, assumes a monosize distribution of aerosol particles, whose radius is assumed to remain constant throughout the simulations. Toon et al. (2007) reported that the typical radii of soot particles range between 50 and 100 nm. Measurements by Reddington et al. (2013) and Wu et al. (2017) indicate that the mass size distribution of BC aerosol peaks around a radius of 100 nm. Reid et al. (2005) pointed out that the size of smoke particles increases with age, with volume median radii growing to average values of around 150 nm. Here a sedimentation radius of 100 nm is used, as also applied in this context by several past studies (e.g., Mills et al., 2008; Pausata et al., 2016; Robock, Oman, Stenchikov, et al., 2007; Robock, Oman, & Stenchikov, 2007; Stenke et al., 2013). Although the atmospheric removal of smaller, 50 nm radius particles is slightly slower (because of the larger surface-to-mass ratio of the particulate), previous work suggests that their impact on the atmosphere state is similar (e.g., Mills et al., 2014; Stenke et al., 2013). In particular, after the initial rainout, the average *e*-folding time scales for the removal of 50 and 100 nm radius particles differ by about 4% in the comparison performed by Mills et al. (2014). Differences in the *e*-folding removal time scales remained small also in the corresponding experiments of Stenke et al. (2013), who concluded that the atmospheric lifetime of soot is not critically impacted by the radius of the particles in this size range.

The optical properties of BC used in WACCM are derived from the Optical Properties of Aerosols and Clouds (OPAC) software package (Hess et al., 1998), based on a soot radius distribution ranging from 5 nm to 20 μm. Experiments by Mills et al. (2014), using the same optical constant database, resulted in very similar anomalies for the net solar flux at the surface when choosing a particle radius of 50 or 100 nm, although Hess et al. (1998) used a soot volume distribution with a mode radius of 50 nm to compute the optical constants. Outcomes from the same study are also consistent with the conclusions of Robock, Oman, Stenchikov, et al. (2007), who used different sources for the soot optical constants. In particular, over the first years, the evolution of the BC optical depth is comparable (see also the OPAC-based simulations of Stenke et al., 2013). Pausata et al. (2016) stressed that in the aftermath of a nuclear exchange, BC can coexist with organic carbon, which has different absorption and scattering coefficients compared to those of BC. Coagulation of these two species can alter the optical properties of the aerosols, although compositional diversity across BC-containing particles is also important for determining the global optical properties of soot. Assuming a population-averaged composition for all particles can overestimate the absorption by as much as a factor of 2 (Fierce et al., 2016). In their 1 day emission scenarios, Pausata et al. (2016) found that the largest net solar flux anomalies at surface ranged from −8 to −15 W/m^2 during the first year, comparable to that obtained in prior work (e.g., Mills et al., 2014; Robock, Oman, Stenchikov, et al., 2007) and in some of our simulations (see section 3.3). Moreover, they found that ensuing particle growth via coagulation can reduce the atmospheric lifetime of the aerosols by 50% compared to the case in which organic carbon is absent.

In these simulations, BC particles can only evolve through transport and deposition. Even though, as mentioned above, coating and aging can alter the optical properties of the resulting aerosols, surface chemistry is neglected, as is the fact that soot particles can exist as fractal aggregates (e.g., China et al., 2013). In particular, deposition through sedimentation is affected in nontrivial ways by the fractal nature of soot. Although the enhanced surface-to-mass ratio of the aggregates may hinder gravitational settling (compared to

spherical particles of equal mass), exposure to, for example, sulfuric acid vapor produces compaction of the aggregates, an effect that increases with aggregate size and facilitates gravitational settling (Zhang et al., 2008). In addition to dry deposition, soot particles undergo wet deposition (see, e.g., Penner & Molenkamp, 1989). Freshly emitted BC particles are generally hydrophobic. However, the hydrophobic-to-hydrophilic conversion time scale of tropospheric carbonaceous aerosols is found to have global averages of a few days and to decrease with altitude (Huang et al., 2013). In the calculations of Robock, Oman, Stenchikov, et al. (2007), it was assumed that the hydrophobic-to-hydrophilic conversion of BC aerosols was essentially completed a few days after the exchange. Alternatively, because of these relatively short conversion times, the hydrophilic approximation (e.g., Mills et al., 2008, 2014), or some similar approximation (Stenke et al., 2013), has often been applied since the beginning of the simulations. As noted by Stenke et al. (2013), this approach may represent an upper bound of the BC wet deposition rate in the troposphere, as it implicitly assumes that soot particles become readily coated. Laboratory studies, however, do indicate that the time scales required by BC aerosols to be coated with hydrophilic materials are short, varying in the range from a few hours to a day (Lambe et al., 2015). In our simulations, BC particles are assumed to be fully hydrophilic upon their injection into the atmosphere and, therefore, to be readily subjected to wet deposition, which results in a relatively rapid rainout in the troposphere. Although a more accurate and physically consistent treatment of BC aerosols would be desirable in this and other contexts (e.g., growth and aging effects on radiative feedback), the fact that particles can be removed by precipitation from the beginning of the simulations does not significantly affect the early evolution of their distribution. Over the first 4 days after the exchange, about 13% of the initial BC burden is removed from the atmosphere (see section 3.3) compared to around 30% reported by Stenke et al. (2013).

The reference, nonforced, climate state was gauged by executing a simulation ensemble of 11 members without the BC aerosol contributed by the exchange. Each ensemble simulation started on 1 January 2013 and ran for 33 model years. The atmospheric configuration followed the specifications of the "medium to low emissions" Representative Concentration Pathway (RCP4.5) scenario for the concentrations of greenhouse gases, including all major anthropogenic sources (Marsh et al., 2013; Meinshausen et al., 2011). Experiments conducted by Mills et al. (2014) indicate that starting the exchange later in the year (e.g., in May) does not produce significant differences in the climate response. The initial conditions for the CESM components were taken from a RCP4.5 run that was part of phase 5 of the Coupled Model Intercomparison Project (Taylor et al., 2012). Mills et al. (2014) used the same initial conditions. Variations across the ensemble members were introduced by applying round-off level differences in the initial air temperature of each member. In members 2 through 11, a random perturbation of the atmospheric temperature field, in the 13th to 14th significant digits, was applied to the air temperature field of member 1. This is the same procedure used to generate ensemble members for the NCAR Large Ensemble Community Project (Kay et al., 2015). Apart from the initial air temperature, all control ensemble members had the same initial conditions.

Similarly, the forced climate state was evaluated by conducting a simulation ensemble of 12 members, in which the atmosphere is regionally loaded with BC aerosol contributed by fires in the aftermath of the exchange. (As noted in section 3.1, contributions from the initial detonations and fireballs are minimal.) Each atmospheric layer was assigned a soot mass taken from the vertical distribution of BC emission, overlapping that layer, produced by the HIGRAD-FIRETEC calculation (see section 3.2). Horizontally, this emission source was added to three grid columns between roughly 27.5°N–67.5°E and 31.3°N–72.5°E over Pakistan and to three grid columns centered around 27.5°N–80°E over India. In the forced climate case, variations across the ensemble members were generated by using a set of vertical profiles of the BC emission spanning 11 min of the fire simulation, each profile taken 1 min apart. The HIGRAD-FIRETEC simulation to estimate the vertical BC distribution was based on a worst case scenario, that is, no rubble and high spotting ignition probabilities. The total magnitude of the BC load emitted in the atmosphere ranged from 3.68×10^9 to 3.72×10^9 kg, or 3.68 to 3.72 Tg (teragram, 10^9 kg). While the bulk of it was released at heights below 12 km (see sections 2.2 and 3.2), 0.20–0.24 Tg of the BC mass reached above 12 km, which is comparable to or larger than the higher estimate made from an actual pyrocumulonimbus formed by a wildfire with a similar burnt area (Fromm et al., 2008). Except for the atmospheric BC loading, the initial conditions of the forced simulations were the same as those applied to member 1 of the control ensemble.

For purposes of validation and comparison, one additional simulation used the initial BC distribution applied in the experiments of Mills et al. (2014), in which 5 Tg of soot was released in the atmosphere between 300

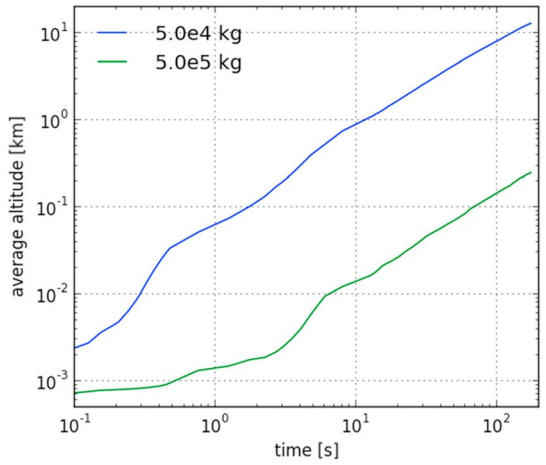

Figure 4. The average altitude of the lofted dirt and debris as a function of time for a single 15 kt source. The blue and green lines represent the average altitude of the uppermost 5×10^4 kg and 5×10^5 kg of material.

and 150 hPa (i.e., in the upper troposphere, roughly between 9 and 14 km), with a constant mass-mixing ratio, over two regions centered on India and Pakistan. A similar initial distribution for the BC was used, among others, by Robock, Oman, Stenchikov, et al. (2007), Mills et al. (2008), Stenke et al. (2013), and Pausata et al. (2016). With this simulation setup, the observed climatic effects are largely similar to those discussed by Mills et al. (2014), although they conducted most of their experiments with 50 nm radius BC particles.

3. Results

This section details results from each of the modeling systems that taken together demonstrate the relatively small impact of a limited exchange of low-yield nuclear weapons between India and Pakistan.

3.1. Fireball Results

Our concern with this part of the modeling system was to ensure that we capture the effects of any debris lofted by the fireball itself as part of our carbon forced scenario. Initially, the fireball expands outward with a strong shock that coincides with the radiating surface. As the fireball expands outward it evacuates the region behind the shock. Initially, the extreme temperatures provide pressure support behind the shock; however, as the fireball evolves the shock decouples from the radiation front and the fireball begins to cool and rise into the atmosphere. When this occurs, the flow near the ground surface reverses toward the center. As this flow converges on the central region below the blast it is drawn upward and entrained in the rising fireball. It is during this latter updraft that most of the ground material is entrained in the fireball, not during the initial outgoing blast.

The simulation was run to 3.5 min, at which point the average height of the cloud was 13 km and beginning to stabilize in altitude. The stabilization altitude obtained in the simulation is consistent with the empirical approximation in Glasstone (1962) of 10–13 km for a 15 kt explosion. Figure 4 displays the altitude to which the dirt and debris material that is entrained in the fireball is lofted into the atmosphere, as a function of time. The blue and green lines represent the average altitude of the uppermost 5×10^4 kg and 5×10^5 kg of entrained dirt and debris as a function of time. The material lofted to the highest altitudes represented by the 5×10^4 kg sample point is entrained into the fireball in the early times and in less than 0.5 s is above the initial 50 m height of burst. The 5×10^5 kg data represent the large quantity of ground material that is swept up in the converging flow at later times. While there is substantially more dirt and debris represented by this material, it is rising much slower and to a much lower final altitude compared to the 5×10^4 kg case.

The total mass of debris that is lofted to an altitude above 5 km at the end of the simulation is approximately 6.3×10^4 kg. This number is approximately a factor of 2 less than the mass of lofted dirt predicted from empirical relationships. Both the calculated mass of 6.3×10^4 kg and the approximate empirical mass of 10^5 kg will have impacts on local fallout, but the total mass of lofted dirt is unlikely to have a significant impact on regional or global climate as it is over 2 orders of magnitude less than the mass of carbon produced by the fire spread associated with the detonation.

3.2. Fire Results

The no-rubble simulation produces a significantly more intense fire, with more fire spread, and consequently a significantly stronger plume with larger amounts of BC reaching into the upper atmosphere than the simulation with rubble, illustrated in Figure 5. While the no-rubble simulation represents the worst case scenario involving vigorous fire activity, only a relatively small amount of carbon makes its way into the stratosphere during the course of the simulation. But while small compared to the surface BC mass, stratospheric BC amounts from the current simulations are significantly higher than what would be expected from burning vegetation such as trees (Heilman et al., 2014); for example, the higher energy density of the building fuels and the initial fluence from the weapon produce an intense response within HIGRAD-FIRETEC with initial updrafts of order 100 m/s in the lower troposphere. Or, in comparison to a mass fire, wildfires will burn only

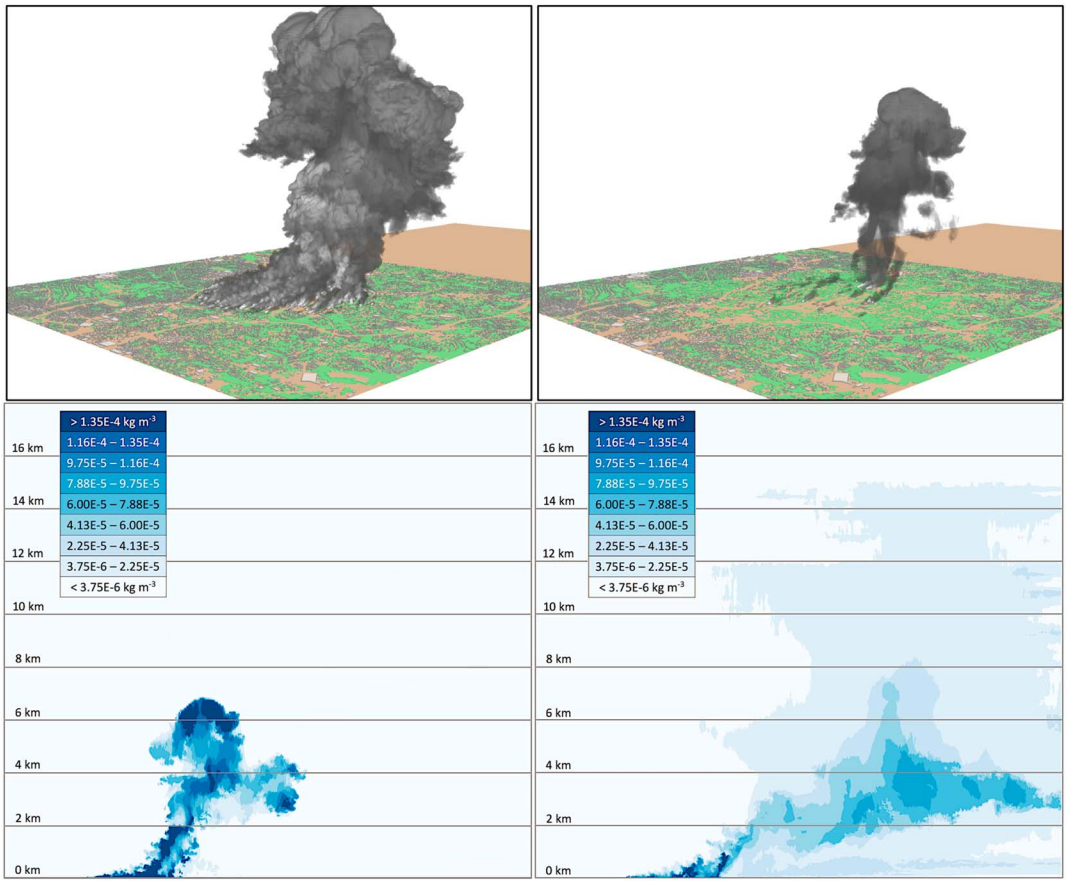

Figure 5. (top left) Isosurfaces of black carbon (BC) (5.625×10^{-6} kg m^{-3}) at 8 min from the no-rubble HIGRAD-FIRETEC simulation. The brown area to the right of the city was added to enable tracking of the plume before it exited. (top right) Isosurfaces of BC (5.625×10^{-6} kg m^{-3}) at 8 min from the rubble HIGRAD-FIRETEC simulation showing much weaker fire behavior. (bottom row) Vertical plane (20 km × 18 km) plots of BC concentration at the center of the domain (at y = 5 km) from the no-rubble HIGRAD-FIRETEC simulation at 8 min (bottom left) and at 20 min (bottom right) after the weapon detonation.

a small amount of fuel in the corresponding time period (roughly 10 min) that a nuclear weapon fluence can effectively ignite a large area of fuel producing an impressive atmospheric response.

Figure 6 shows vertical profiles of BC multiplied by 100 (number of cities involved in the exchange) from the two simulations. The total amount of BC produced is in line with previous estimates (about 3.69 Tg from no-rubble simulation); however, the majority of BC resides below the stratosphere (3.46 Tg below 12 km) and can be readily impacted by scavenging from precipitation either via pyrocumulonimbus produced by the fire itself (not modeled) or other synoptic weather systems. While the impact on climate of these more realistic profiles will be explored in the next section, it should be mentioned that these estimates are still at the high end, considering the inherent simplifications in the combustion model that lead to overestimating BC production.

3.3. Climate Results

Long-term climatic effects critically depend on the initial injection height of the soot, with larger quantities reaching the upper troposphere/lower stratosphere inducing a greater cooling impact because of longer residence times (Robock, Oman, Stenchikov, et al., 2007). Absorption of solar radiation by the BC aerosol and its subsequent radiative cooling tends to heat the surrounding air, driving an initial upward diffusion of the soot plumes, an effect that depends on the initial aerosol concentrations. Mixing and sedimentation tend to reduce this process, and low-altitude emissions are also significantly impacted by precipitation if aging of the BC aerosol occurs on sufficiently rapid time scales. But once at stratospheric altitudes, aerosol dilution

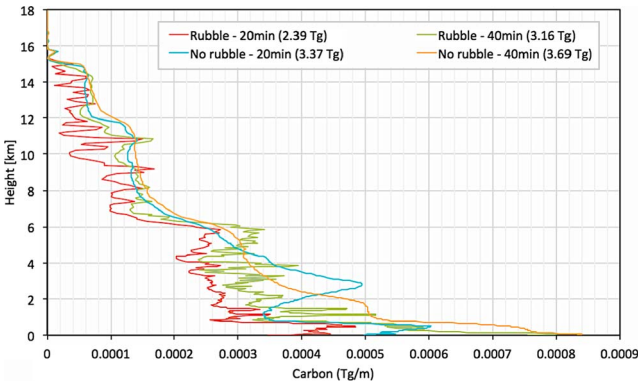

Figure 6. Vertical profiles of the carbon mass per unit height (in Tg/m) from the HIGRAD-FIRETEC simulations, at 20 and 40 min after detonation, from both the no-rubble (blue and orange lines) and the rubble simulations (red and green lines). The total carbon mass for each distribution profile, integrated over the 18 km high domain, is given in the legend. Note that a majority of black carbon is found significantly below the tropopause (roughly 12 km) and hence can be easily washed away by precipitation produced by the climate model. Note that the Mills et al. (2014) distribution would be a vertical line at 0.0011 Tg/m between 9.16 and 13.6 km.

via coagulation is hindered by low particulate concentrations (e.g., Robock, Oman, Stenchikov, et al., 2007) and lofting to much higher altitudes is inhibited by gravitational settling in the low-density air (Stenke et al., 2013), resulting in more stable BC concentrations over long times.

Of the initial BC mass released in the atmosphere, most of which is emitted below 9 km, 70% rains out within the first month and 78%, or about 2.9 Tg, is removed within the first 2 months (Figure 7, solid line), with the remainder (about 0.8 Tg, dashed line) being transported above about 12 km (200 hPa) within the first week. This outcome differs from the findings of, for example, Stenke et al. (2013) (their high BC-load cases) and Mills et al. (2014), who found that most of the BC mass (between 60 and 70%) is lifted in the stratosphere within the first couple of weeks. This can also be seen in Figure 8 (red lines) and in Figure 9, which include results from our calculation with the initial BC distribution from Mills et al. (2014). In that case, only 30% of the initial BC mass rains out in the troposphere during the first 2 weeks after the exchange, with the remainder rising to the stratosphere. In the study of Mills et al. (2008) this percentage is somewhat smaller, about 20%, and smaller still in the experiments of Robock, Oman, Stenchikov, et al. (2007), in which the soot is initially emitted in the upper troposphere or higher. In Figure 7, the *e*-folding time scale for the removal of tropospheric soot, here interpreted as the time required for an initial drop of a factor *e*, is about 1 week. This result compares favorably with the "LT" experiment of Robock, Oman, Stenchikov, et al. (2007), considering 5 Tg of BC released in the lower troposphere, in which 50% of the aerosols are removed within 2 weeks. By contrast, the initial *e*-folding time scale for the removal of stratospheric soot in Figure 8 is about 4.2 years (blue solid line), compared to about 8.4 years for the calculation using Mills et al. (2014) initial BC emission (red solid line). The removal time scale from our forced ensemble simulations is close to those obtained by Mills et al. (2008) in their 1 Tg experiment, by Robock, Oman, Stenchikov, et al. (2007) in their experiment "UT 1 Tg," and by Stenke et al. (2013) in their experiment "Exp1," in all of which 1 Tg of soot was emitted in the atmosphere in the aftermath of the exchange. Notably, the *e*-folding time scale for the decline of the BC mass in Figure 8 (blue solid line) is also close to the value of about 4 years quoted by Pausata et al. (2016) for their long-term "intermediate" scenario. In that scenario, which is also based on 5 Tg of soot initially distributed as in Mills et al. (2014), the factor-of-2 shorter residence time of the aerosols is caused by particle growth via coagulation of BC with organic carbon.

Figure 9 shows the BC mass-mixing ratio, horizontally averaged over the globe, as a function of atmospheric pressure (height) and time. The BC distributions used in our simulations imply that the upward transport of particles is substantially less efficient compared to the case in which 5 Tg of BC is directly injected into the upper troposphere. The semiannual cycle of lofting and sinking of the aerosols is associated with atmospheric heating and cooling during the solstice in each hemisphere (Robock, Oman, Stenchikov, et al., 2007). During the first year, the oscillation amplitude in our forced ensemble simulations is particularly large during the summer solstice, compared to that during the winter solstice (see Figure 9, bottom), because of the higher soot concentrations in the Northern Hemisphere, as can be seen in Figure 11 (see also Figure 12, left). Comparing the top and bottom panels of Figure 9, the BC reaches the highest altitudes during the first year in both cases, but the concentrations at 0.1 hPa in the top panel can be 200 times as large. Qualitatively, the difference can be understood in terms of the air temperature increase caused by BC radiation emission, which is several tens of kelvin degrees in the simulations of Robock, Oman, Stenchikov, et al. (2007) (see their Figure 4), Mills et al. (2008) (see their Figure 5), Stenke et al. (2013 (see high-load cases in their Figure 4), Mills et al. (2014) (see their Figure 7), and Pausata et al. (2016) (see 1 day emission cases in their Figure 1), due to high BC concentrations, but it amounts to only about 10 K in our forced ensemble simulations, as illustrated in Figure 10. Results similar to those presented in Figure 10 were obtained from the experiment "Exp1" performed by Stenke et al. (2013) (see their Figure 4). In that scenario as well, somewhat less than 1 Tg of BC remained in the atmosphere after the initial rainout.

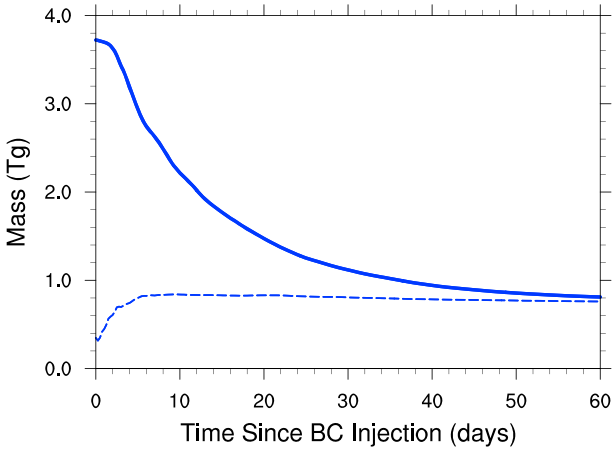

Figure 7. Black carbon (BC) mass as a function of time, over the first 60 days after the exchange, for the forced simulation with largest BC atmospheric load (3.72 Tg). The solid line represents the total mass, whereas the dashed line represents the mass at heights above 200 hPa (about 12 km). The amount of BC advected above 12 km increases by about 2.5 times over the first week or so. However, most of the BC mass remains at lower altitudes, leading to a significant decline over the following weeks because of both fallout and rainout (BC aerosols undergo wet deposition). Note that only a relatively small amount of BC is removed over the first few days, when the conversion from hydrophobic to hydrophilic aerosols would occur.

As mentioned before, the BC aerosol that remains in the atmosphere, lifted to stratospheric heights by the rising soot plumes, undergoes sedimentation over a time scale of several years (Figures 8 and 9). This mass represents the effective amount of BC that can force climatic changes over multiyear time scales. In the forced ensemble simulations, it is about 0.8 Tg after the initial rainout, whereas it is about 3.4 Tg in the simulation with an initial soot distribution as in Mills et al. (2014). Our more realistic source simulation involves the worst case assumption of no-rubble (along with other assumptions) and hence serves as an upper bound for the impact on climate. As mentioned above and further discussed below, our scenario induces perturbations on the climate system similar to those found in previous studies in which the climatic response was driven by roughly 1 Tg of soot rising to stratospheric heights following the exchange.

Figure 11 illustrates the vertically integrated mass-mixing ratio of BC over the globe, at various times after the exchange for the simulation using the initial BC distribution of Mills et al. (2014) (Figure 11, top row) and as an average from the forced ensemble members (Figure 11, bottom row). All simulations predict enhanced concentrations at high latitudes during the first year after the exchange. In the cases shown in the top row, however, these high concentrations persist for several years (see also Figure 1 of Mills et al., 2014), whereas the forced ensemble simulations indicate that the BC concentration starts to decline after the first year. In fact, in the simulation represented in the top row, mass-mixing ratios larger than about 1 kg of BC per teragram of air persist for well over 10 years after the exchange, whereas they only last for 3 years in our forced simulations (compare top and middle panels of Figure 9). After the first year, values drop below 3 kg BC/Tg air, whereas it takes about 8 years to reach these values in the simulation in the top row (see also Robock, Oman, Stenchikov, et al., 2007). Over crop-producing, midlatitude regions in the Northern Hemisphere, the BC loading is reduced from more than 0.8 kg BC/Tg air in the simulation in the top row to 0.2–0.4 kg BC/Tg air in our forced simulations (see middle and right columns).

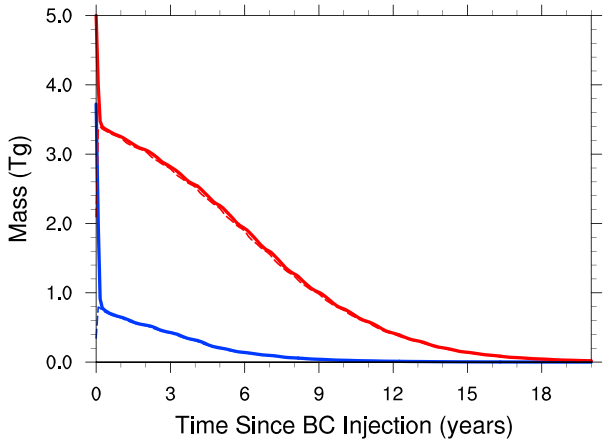

Figure 8. Total black carbon (BC) mass versus time as an average from the forced ensemble simulations (solid blue line) and from the simulation with an initial BC distribution as in Mills et al. (2014) (solid red line). The dashed lines represent the mass at heights above 200 hPa (about 12 km). Most of the mass remaining after the first month resides above 12 km, and much less remains in the simulations represented by the blue line than does in the simulation represented by the red line.

The more rapid clearing of the atmosphere in the forced ensemble is also signaled by the soot optical depth in the visible radiation spectrum, which drops below values of 0.03 toward the second half of the first year at midlatitudes in the Northern Hemisphere and everywhere on the globe after about 2.5 years (without ever attaining this value in the Southern Hemisphere). In contrast, the soot optical depth in the calculation shown in the top row of Figure 11 becomes smaller than 0.03 everywhere only after about 10 years. The two cases show a similar tendency, in that the BC optical depth is typically lower between latitudes 30°S–30°N than it is at other latitudes. This behavior is associated to the persistence of stratospheric soot toward high-latitudes and the Arctic/Antarctic regions, as illustrated by the zonally averaged, column-integrated mass-mixing ratio of the BC in Figure 12 for both the forced ensemble simulations (left panel) and the simulation with an initial 5 Tg BC emission in the upper troposphere (right panel).

The spread in the globally averaged (near) surface temperature of the atmosphere, from the control (left panel) and forced (right panel) ensembles, is displayed in Figure 13. For each month, the plots show the largest variations (i.e., maximum and minimum values), within each ensemble of values obtained for that month, relative to the mean value of that month. The plot also shows yearly averaged data (thinner lines). The spread is comparable in the control and forced ensembles, with

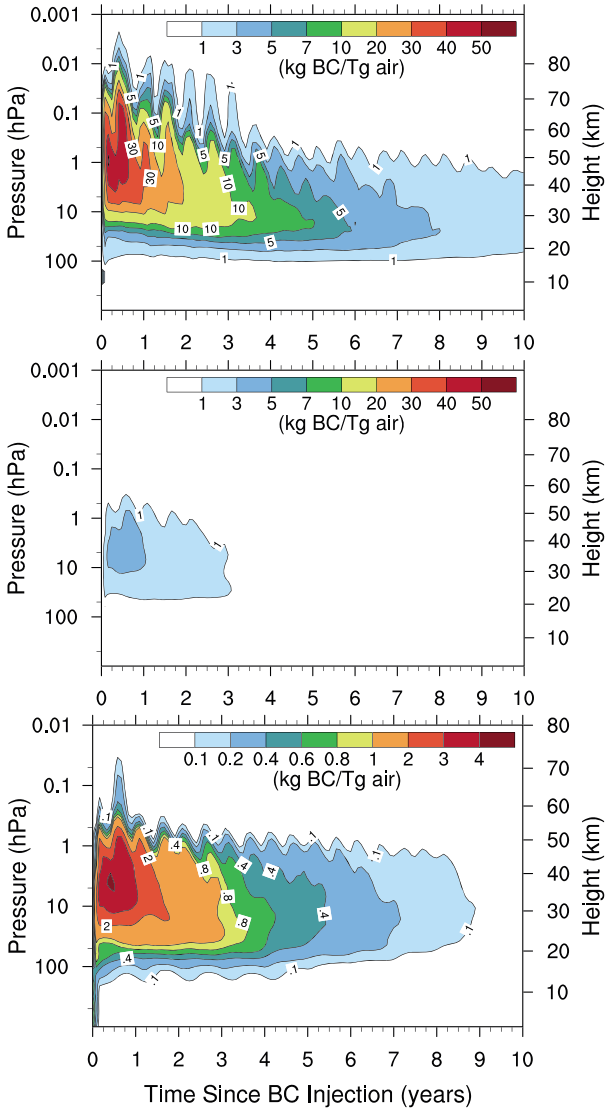

Figure 9. Black carbon (BC) mass-mixing ratio, horizontally averaged over the globe, as a function of atmospheric pressure and time. (top) Simulation using the initial source distribution as in Mills et al. (2014), plotted on the scale shown in the middle panel for ease of comparison. (middle) As in the top panel, for our forced ensemble. The average includes all members of the forced ensemble. (bottom) Same information as in the middle panel, plotted using a more detailed scale. As a reference, the initial BC load is mostly distributed below 12 km. Large concentrations (e.g., around heights of 40 km) are also determined by the reduced air density.

average values calculated over the 33 year run length of 0.4–0.5 K. This spread is also similar to the internal variability of the globally averaged surface temperature quoted for the NCAR Large Ensemble Community Project (Kay et al., 2015). These results imply that surface air temperature differences, between forced and control simulations, which lie within the spread, may not be distinguished from effects due to internal variability of the two simulation ensembles.

Figure 14 shows the difference in the globally averaged surface temperature of the atmosphere (top panel), net solar radiation flux at surface (middle panel), and precipitation rate (bottom panel), computed as the (forced minus control) difference in ensemble mean values. The sum of standard deviations from each ensemble is shaded. Differences are qualitatively significant over the first few years, when the anomalies lie near or outside the total standard deviation. Inside the shaded region, differences may not be distinguished from those arising from the internal variability of one or both ensembles. The surface solar flux (middle panel) is the quantity that appears most affected by the BC emission, with qualitatively significant differences persisting for about 5 years. The precipitation rate (bottom panel) is instead affected only at the very beginning of the simulations. The red lines in all panels show the results from the simulation applying the initial BC distribution of Mills et al. (2014), where the period of significant impact is much longer owing to the higher altitude of the initial soot distribution that results in longer residence times of the BC aerosol in the atmosphere. When yearly averages of the same quantities are performed over the India-Pakistan region, the differences in ensemble mean values lie within the total standard deviations of the two ensembles.

The results in Figure 14 can also be compared to the outcomes of other previous studies. In their experiment "UT 1 Tg," Robock, Oman, Stenchikov, et al. (2007) found that when only 1 Tg of soot remains in the atmosphere after the initial rainout, temperature and precipitation anomalies are about 20% of those obtained from their standard 5 Tg BC emission case. Therefore, the largest differences they observed, during the first few years after the exchange, were about −0.3 K and −0.06 mm/day, respectively, comparable to the anomalies in the top and bottom panels of Figure 14. Their standard 5 Tg emission case resulted in a solar radiation flux anomaly at surface of −12 W/m^2 after the second year (see their Figure 3), between 5 and 6 times as large as the corresponding anomalies from our ensembles shown in the middle panel. In their experiment "Exp1," Stenke et al. (2013) reported global mean surface temperature anomalies not exceeding about 0.3 K in magnitude and precipitation anomalies hovering around −0.07 mm/day during the first few years, again consistent with the results of Figure 14.

In a recent study, Pausata et al. (2016) considered the effects of an admixture of BC and organic carbon aerosols, both of which would be emitted in the atmosphere in the aftermath of a nuclear exchange. In particular, they concentrated on the effects of coagulation of these aerosol species and examined their climatic impacts. The initial BC distribution was as in Mills et al. (2014), although the soot burden was released in the atmosphere over time periods of various lengths. Most relevant to our and other previous work are their 1 day emission scenarios. They found that during the first year, the largest values of the atmospheric surface temperature anomalies ranged between about −0.5 and −1.3 K, those of the sea surface temperature (SST) anomalies ranged between −0.2 and −0.55 K, and those of the precipitation anomalies varied between −0.15 and −0.2 mm/d. All these ranges are compatible with our results shown in Figure 14 as red lines

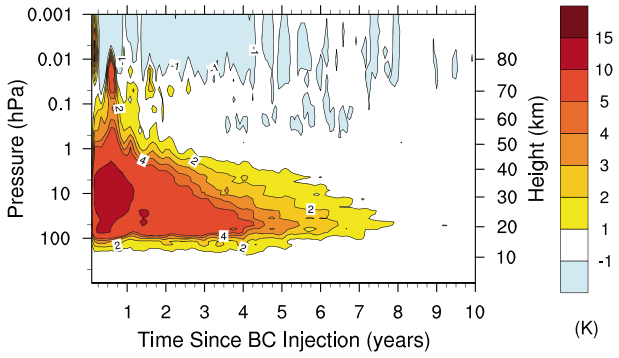

Figure 10. Evolution of the vertical air temperature anomaly, horizontally averaged over the globe. The difference is calculated from the averages of the forced and control ensembles. The maximum increase in temperature, between 20 and 40 km, is about 10 K. The plot should be compared, for example, to Figure 4 of Robock, Oman, Stenchikov, et al. (2007), to Figure 5 of Mills et al. (2008), and to Figure 7 of Mills et al. (2014), in which air temperatures rise by 50 K or more. These results show similarities with those of the experiment "Exp1" of Stenke et al. (2013) (see their Figure 4).

and with those of Mills et al. (2014) (see their Figures 3 and 6). As already mentioned in section 2.3, the net solar flux anomalies at surface are also consistent. This overall agreement suggests that the inclusion of organic carbon aerosols, and ensuing coagulation with BC, should not dramatically alter the climatic effects resulting from our forced ensemble simulations. Moreover, aerosol growth would likely shorten the residence time of the BC particulate in the atmosphere (Pausata et al., 2016), possibly reducing the duration of these effects.

3.4. Statistical Significance of Climate Impacts

To determine the statistical similarity of the control and forced ensembles, statistical emulators for each ensemble were developed. We focus on time series of globally averaged near-surface air temperature and SST, removing a baseline seasonal cycle from each simulation using the climatology calculated from the control ensemble (see Figure 15). For each simulation, we fit an autoregressive moving average model (e.g., Whittle, 1983),

$$X(t) = \sum_{i=1}^{p} a(i)X(t-i) + \sum_{i=1}^{q} b(i)\varepsilon(t-i) + \varepsilon(t)$$

where p is the number of autoregressive terms, q is the number of moving average terms, ε is Gaussian white noise with variance σ^2, and a and b are model parameters. We determine the optimal order (p, q) by the Akaike Information Criterion (Akaike, 1974), using the largest optimal order among all ensemble members for all models. We then create a super ensemble for each of the control and forced ensembles by generating 100 realizations from each autoregressive moving average model. This allows us to calculate confidence intervals around a mean trajectory for the control and forced ensembles, in order to determine when the two ensembles differ in a statistically significant manner.

Figure 16 displays the results of the statistical emulators. The models initially deviate from each other in both near-surface temperature and SST (during years 1–3), when each model's mean is near or outside the other's 95% confidence interval. During this period, the ensembles are statistically different. For the remainder of the simulation, however, the model means are well within each other's confidence intervals and are thus statistically similar. This is also true for the ocean surface temperature, which evolves on longer time scales than does the atmosphere surface temperature.

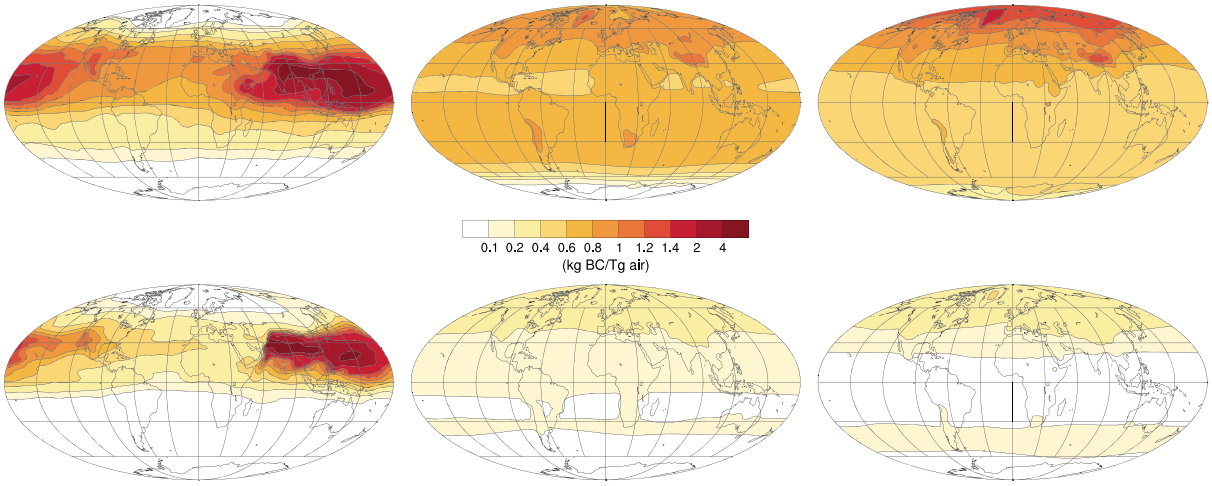

Figure 11. Vertically integrated, monthly averaged black carbon (BC) mass-mixing ratio over the globe for three different months: (from left to right columns) month 1, month 6, and month 12 after the exchange. The top row refers to the simulation with the BC distribution used by Mills et al. (2014), whereas the bottom row refers to the average mass-mixing ratio from our forced ensemble simulations.

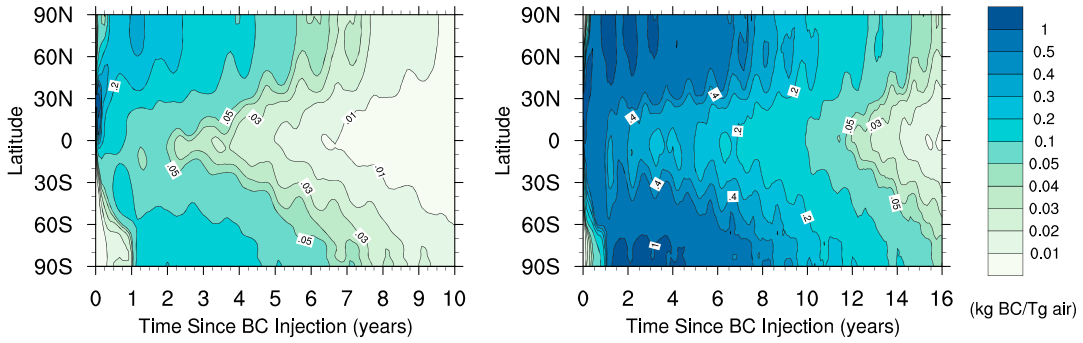

Figure 12. The plots show the black carbon (BC) mass-mixing ratio, zonally averaged and vertically integrated, as a function of latitude and time. (left) Averaged from the forced ensemble simulations and (right) the result from the simulation with an initial 5 Tg emission of soot in the upper troposphere. In both cases, removal of the soot particulate is faster in a wide band around the equator, as can also be inferred from the optical depth maps of Robock, Oman, Stenchikov, et al. (2007), Stenke et al. (2013), and Mills et al. (2014).

By examining the spatial map of differences in 5 year averaged near-surface air temperature in Figure 17 (top left), we see that the overall cooling of the forced ensemble relative to the control ensemble, shown above in Figures 14 and 16, is in fact associated with a statistically significant cooling over most of the globe, most notably in the polar regions. Over the Indian subcontinent, differences are generally not significant. Toward the end of the simulations, about 30 years after the exchange, when there is no appreciable difference in the global mean near-surface air temperatures (see Figures 14 and 16), regional differences remain significant at the 95% level (Figure 17, top right). As the strong uniform cooling signal observed at early times in the simulations fades, regional interannual variability in near-surface temperature differences may persist for the remainder of the simulations (not shown), with statistically significant differences over the last 5 years largely restricted to the oceans (top right).

During years 2–6, the precipitation differences appear to be particularly significant at high latitudes, especially over the Arctic where the forced ensemble tends to be drier (Figure 17, bottom left). Toward the end of the simulations, the areas of significant difference in precipitation are modest in extent (Figure 17, bottom right). The precipitation difference over a portion of the Western Pacific Warm Pool, where precipitation rates are high, is statistically significant at latitudes south of the equator throughout the simulations with strong interannual variability.

We hypothesize that differences near the end of the calculations are due to a temporal phase shift in global-scale climate oscillations, such as the El Nino–Southern Oscillation. Fully understanding these differences and their local impacts requires further analysis, which we plan for a future publication.

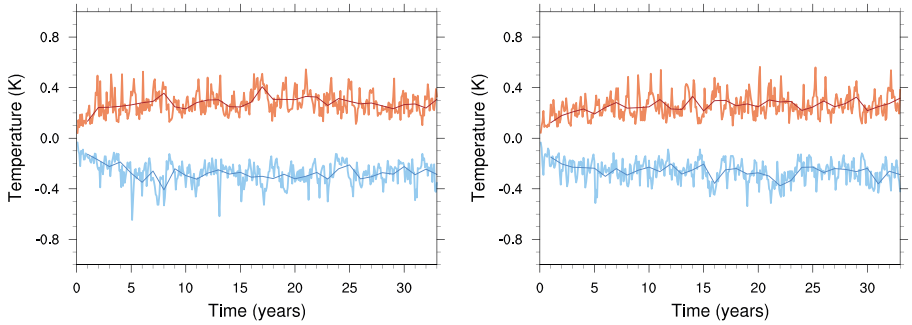

Figure 13. Global mean near-surface air temperature spread, across ensemble members, where the mean value from the ensemble has been removed (see text for additional details). The spread is computed as the maximum (positive and negative) deviations from the mean. The plots are produced from monthly averaged data. (left) Results from the control ensemble. (right) Results from the forced ensemble. The overall spread in the two ensembles is similar. The thinner solid lines represent annually averaged values.

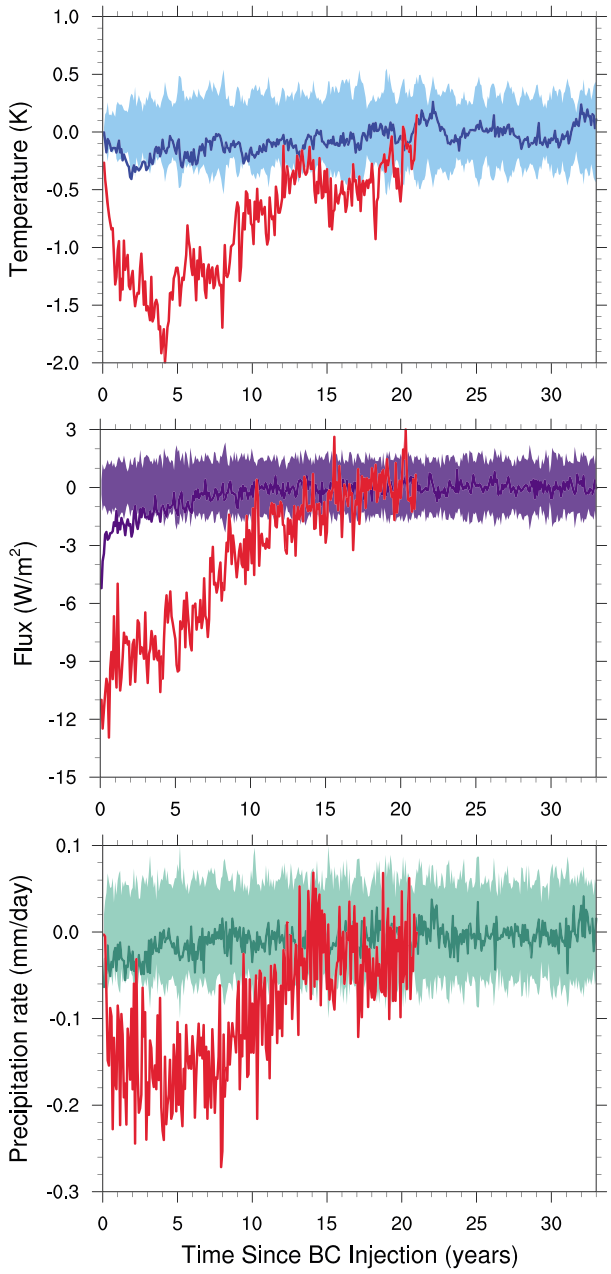

Figure 14. Ensemble mean anomalies (forced minus control), globally averaged over the globe, for the near-surface atmospheric temperature (top), net solar radiation flux (middle), and precipitation rate (bottom). The red lines are corresponding results from the simulation applying the same black carbon (BC) source as in Mills et al. (2014). Shading represents the spread in total standard deviation (forced plus control) relative to the ensemble means. The plots are produced from monthly averaged data.

4. Discussion

Fires initiated by warhead detonations can induce mass fires into the local urban environment, producing aerosols and soot particles. While we chose a U.S. city to burn down, we were conservative in terms of producing a quantity of soot at the high end of the range of what might occur in an actual scenario (no rubble) and believe this still to be the case for a city in India or Pakistan. The fire simulation produced a vertical profile of the carbon concentration from the Earth's surface through the troposphere and into the stratosphere. This profile was input into the same global Earth system model (CESM) used by Mills et al. (2014), at a single point in time. CESM's global transport and atmospheric chemistry mechanisms complete the chemical transport and evolution for the globe.

To quantitatively account for natural and forced variability in the climate system, we created two ensembles, one for the natural, unforced system and a second ensemble using a range of realistic vertical profiles for the BC aerosol forcing, consistent with our detailed fire simulation. The control ensemble was generated using small atmospheric temperature perturbations (Kay et al., 2015). Notably, the overall spread of anomalies in both ensembles is very similar. These ensembles were then used to create "super ensembles" using a statistical emulator, which allows a robust statistical comparison of our simulated results with and without the carbon forcing.

Our primary result is the decreased impact on global climate indices, such as global average surface temperature and precipitation, relative to standard scenarios considered in previous work (e.g., Mills et al., 2014; Pausata et al., 2016; Robock, Oman, Stenchikov, et al., 2007; Stenke et al., 2013). With our finding of substantially less BC aerosol being lofted to stratospheric heights (e.g., over a factor of 4 less than in most of the scenarios considered by previous studies), these globally averaged anomalies drop to statistically insignificant levels after the first several years (Figures 14 and 16). Our results are generally comparable to those predicted by other studies that considered exchange scenarios in which only about 1 Tg of soot is emitted in the upper troposphere (Mills et al., 2008; Robock, Oman, Stenchikov, et al., 2007; Stenke et al., 2013). There are more subtle suggestions of regional effects, notably in the extent of the region over which SST differences between ensembles remain significant in the final years of simulation (Figure 17). Further work is required to adequately analyze these and other potential regional effects.

Historical analysis of several large volcanic eruptions and a recent large fire also supports this result. For example, Timmreck et al. (2010) claim that nonlinear aerosol effects of the Toba Tuff eruption 74,000 years ago helped limit significant global cooling impacts to a 2 year time period and that any cooling beyond this time period could be due to other effects. It should be noted that this eruption was estimated to have produced 10^6 Tg of ash and comparable amounts of other gases, such as sulfur dioxide (SO_2), while the estimated amount of soot produced by a regional exchange is on the order of 10 Tg or 5 orders of magnitude smaller than the ash (not including gases) produced by the Toba eruption. Noting that a nuclear exchange is not identical to volcanic events, it has been asserted that BC particles produced by fires should have a greater impact on absorbing solar radiation than even has the significantly larger amounts of ash and various gases produced by large eruptions (e.g., Robock & Toon, 2010). Likewise, recent work in analyzing BC emissions from large fires suggests that in such fires,

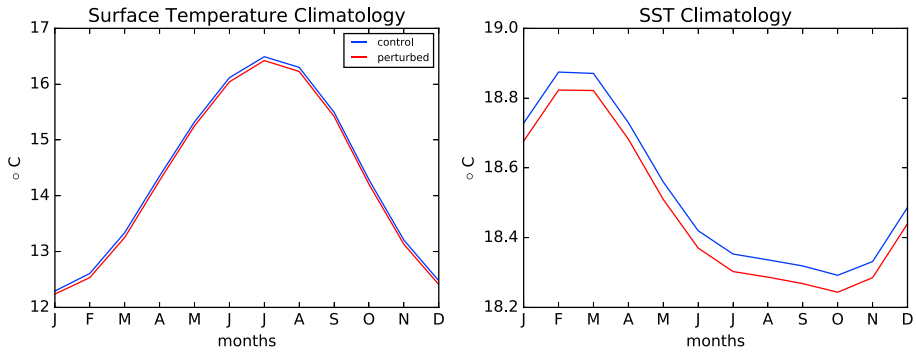

Figure 15. Monthly global climatology for the near-surface air temperature (left) and for the sea surface temperature (SST, right) obtained from the control and forced ensemble simulations, averaged over the members of each ensemble and all years of the simulations.

similar to large volcanic eruptions, coating of soot particles with other particles in convective eddies tends to increase their size and hence increase their subsequent rainout (China et al., 2013) before they can reach the stratosphere. In fact, the recent study of Pausata et al. (2016) found that growth of BC aerosol via coagulation with organic carbon significantly reduces the particles' lifetime in the atmosphere.

One source of error in our study is the linkage between HIGRAD-FIRETEC and CESM. In particular, regional climate simulations are needed to fill in the rather large, disparate spatial scales between the two modeling systems, and to understand how small-scale, synoptic weather conditions influence the movement of BC

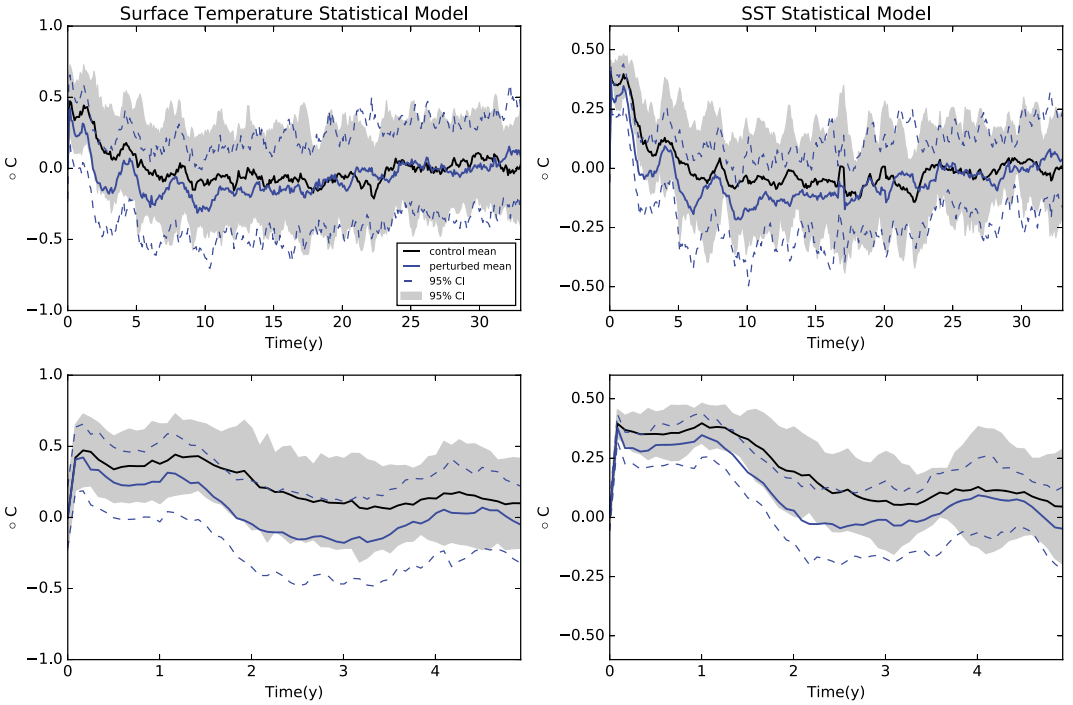

Figure 16. Statistical models for the control and forced ensemble anomalies, relative to the control ensemble climatology for near-surface air temperature (left) and SST (right). (bottom row) A closer view of the first 5 years. The solid black (control) and solid blue (forced) lines are means from a super ensemble generated by 100 realizations of autoregressive moving average models fit to each ensemble member. The associated 95% confidence intervals are indicated by gray shading, corresponding to the control mean (solid black line), and by dashed blue lines, corresponding to perturbed mean (solid blue line). The statistical models deviate significantly between years 1 and 3, indicated by the forced model mean lying near or outside the 95% confidence interval of the control model, and vice versa. Beyond this initial time frame, the ensemble members are statistically similar.

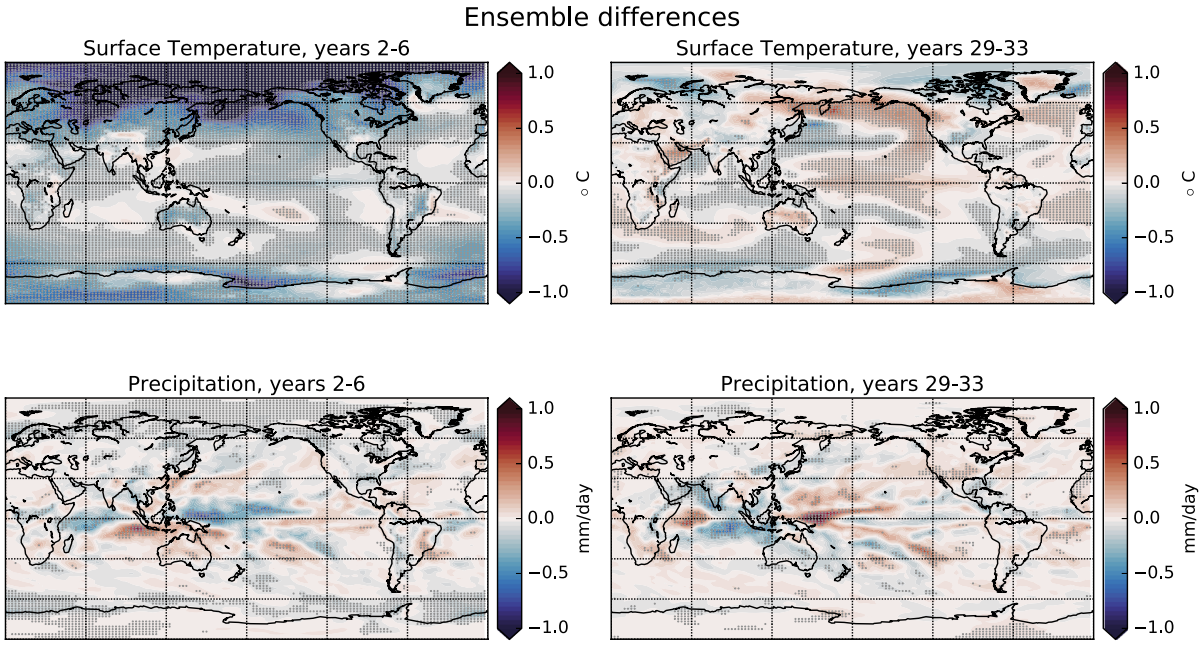

Figure 17. Differences in near-surface air temperature (top row) and precipitation (bottom row) of the perturbed ensemble relative to the control ensemble, averaged over 5 year periods at the beginning (left column) and at the end (right column) of the simulations. Hatching represents differences that are statistically significant at the 95% level, as determined by the Welch's *t* test (e.g., Ruxton, 2006).

particles into the stratosphere. For instance, regional climate simulations should be better able to address the role of turbulent mixing and cloud rainout in dispersing the BC plumes from the various cities over the India-Pakistan region and hence provide a more realistic source to CESM. Another issue that could be addressed by regional climate simulations is the potential impact of the exchange on the Indian monsoon, for example, whether the reduction in surface heating is sufficient to either delay or prevent its formation.

5. Conclusions

There have recently been new simulations of a limited nuclear exchange in the India-Pakistan region using modern climate models (e.g., Mills et al., 2014; Stenke et al., 2013) that suggest devastating impacts on climate over a decadal time scale, although somewhat less extreme consequences have also been suggested (Pausata et al., 2016). Our team has taken a careful look at some of the assumptions that were used in those studies, using an end-to-end modeling sequence. Our series of simulations started with a nuclear weapon explosion followed by a simulation of the fireball and cloud rise. The key improvement in this study is our simulation of fire spread and soot transport in the environment that results from fires initiated by the fireball.

Due to the heat of the fire and of the BC particles that are produced, some of the particles are lofted into the stratosphere. However, our comprehensive urban fire simulations indicate that the bulk of the carbon mass remains in the troposphere, where it is quickly removed from the atmosphere. In most previous work, for example, that of Stenke et al. (2013) and Mills et al. (2014), all of the soot produced by the urban fires is directly injected near the top of the troposphere, and therefore much of it rises into the stratosphere, where it shades and cools the Earth. In contrast, if we use a realistic vertical profile for the BC aerosols as input to the climate model, the long-term global impacts on climate are much less severe than predicted by previous studies. This was true even with conservative, worst case assumptions regarding BC production.

To assess the significance of differences between a limited nuclear exchange scenario and the control climate, we created an ensemble of forced (BC-loaded) simulations using a range of realistic vertical emission profiles, all consistent with our detailed fire simulation. A similar ensemble generated using small atmospheric temperature perturbations allows a robust statistical comparison of our simulated results with and without the carbon forcing. This analysis demonstrates that while modest, statistically significant

differences occur during the first few years, longer-term impacts are unlikely, regional in scope, and limited in scale. None of the simulations produced a nuclear winter effect.

We also completed a thorough nuclear weapon simulation, determining that it was not necessary for this study and that the impact on climate of the fireball and cloud rise is negligible. There are other, worse effects than those on climate, however, such as nuclear fallout in the region. Such consequences will be the focus of our future work using both xRage and HIGRAD-FIRETEC. Likewise, we will conduct a more comprehensive investigation of regional effects, such as potential consequences for the Asian monsoon during the first few years after the nuclear exchange in follow-on work. Additionally, although this study examines a possible exchange between India and Pakistan via the injection of soot over this region, our modeling system could be used to examine potential impacts of other regional exchange scenarios.

Acknowledgments

This work was done under the auspices of the National Nuclear Security Administration of the U.S. Department of Energy at Los Alamos National Laboratory under contract DE-AC52-06NA25396. The CESM project is supported by the National Science Foundation and the Office of Science, Biological and Environmental Research of the U.S. Department of Energy. Computing resources were provided by the High-Performance Computing Division and Institutional Computing at LANL as well as by the U.S. Department of Defense. Special thanks go to members of a LANL computing committee that enabled a special queue for calculation of the CESM ensemble members. Data for the figures produced by CESM as well as the CESM code and input decks can be moved to the Earth System Grid and accessed via that platform (https://www.earthsystemgrid.org/); xRage and HIGRAD-FIRETEC are export controlled models, and input decks and data can be requested via LANL's Richard P. Feynman Center for Innovation (feynmancenter@lanl.gov).

References

Akaike, H. (1974). A new look at the statistical model identification. *IEEE Transactions on Automatic Control*, *19*(6), 716–723. https://doi.org/10.1109/TAC.1974.1100705

Anderson, H. E. (1982). Aids to determining fuel models for estimating fire behavior, USDA Forest Service, Intermountain Forest and Range Experiment Station. General Technical Report, INT-122, 22 p.

Bradley, P. A., Cobble, J. A., Tegillis, I. L., Schmitt, M. J., Obrey, K. D., Glebov, V., et al. (2012). Role of shocks and mix caused by capsule defects. *Physics of Plasmas*, *21*. https://doi.org/10.1063/1.4752014

Bukowski, R. W. (2006). Determining design fires for design-level and extreme events, In Proceedings of the 6th International Conference on Performance Based Codes and Fire Safety Design Methods, Tokyo, Japan, 14–16.

Canfield, J. M., Linn, R. R., Sauer, J. A., Finney, M., & Forthofer, J. (2014). A numerical investigation of the interplay between fireline length, geometry, and rate of spread. *Agricultural and Forest Meteorology*, *189–190*(1), 48–59.

China, S., Mazzoleni, C., Gorkowski, K., Aiken, A. C., & Dubey, M. K. (2013). Morphology and mixing state of individual freshly emitted wildfire carbonaceous particles. *Nature Communications*, *4*, 2122. https://doi.org/10.1038/ncomms3122

Coen, J. L., Cameron, M., Michalakes, J., Patton, E. G., Riggan, P. J., & Yedinak, K. M. (2013). WRF-Fire: Coupled weather–wildland fire modeling with the weather research and forecasting model. *Journal of Applied Meteorology and Climatology*, *52*(1), 16–38. https://doi.org/10.1175/JAMC-D-12-023.1

Crutzen, P. J., & Birks, J. W. (1982). The atmosphere after a nuclear war: Twilight at noon. *Ambio*, *11*, 114–125.

Danabasoglu, G., Bates, S. C., Briegleb, B. P., Jayne, S. R., Jochum, M., Large, W. G., et al. (2012). The CCSM4 ocean component. *Journal of Climate*, *25*(5), 1361–1389. https://doi.org/10.1175/JCLI-D-11-00091.1

Doss, F. W., Loomis, E. N., Sherrill, L. W., Fincke, J. R., Flippo, K. A., & Keiter, P. A. (2013). Instability, mixing, and transition to turbulence in a laser-driven counterflowing shear experiment. *Physics of Plasmas*, *20*(1), 012707. https://doi.org/10.1063/1.4789618

Fierce, L., Bond, T. C., Bauer, S. E., Mena, F., & Riemer, N. (2016). Black carbon absorption at the global scale is affected by particle-scale diversity. *Nature Communications*, *7*, 12361. https://doi.org/10.1038/ncomms12361

Fierro, A., & Reisner, J. M. (2010). High-resolution simulation of the electrification and lightning of Hurricane Rita during the period of rapid intensification. *Journal of the Atmospheric Sciences*, *68*, 477–494.

Frey, L., Even, W., Whalen, D. J., Fryer, C. L., Hungerford, A. L., Fontes, C. J., & Colgan, J. (2013). The Los-Alamos supernova project light-curve project: Computational methods. *The Astrophysical Journal Supplement*, *204*(2), 1–18.

Fromm, M., Torres, O., Diner, D., Lindsey, D., Vant Hull, B., Servranckx, R., et al. (2008). Stratospheric impact of the Chisholm pyrocumulonimbus eruption: 1. Earth-viewing satellite perspective. *Journal of Geophysical Research*, *113*, D08202. https://doi.org/10.1029/2007JD009153

Gent, P. R., Danabasoglu, G., Donner, L. J., Holland, M. M., Hunke, E. C., Jayne, S. R., et al. (2011). The Community Climate System Model version 4. *Journal of Climate*, *24*(19), 4973–4991. https://doi.org/10.1175/2011JCLI4083.1

Gittings, M., Weaver, R., Clover, M., Betlach, T., Byrne, N., Coker, R., et al. (2008). The RAGE radiation-hydrodynamics code. *Computational Science & Discovery*, *1*, 1–60.

Glasstone, S. (1962). *The Effects of Nuclear Weapons* (p. 730). Washington, DC: United States Atomic Energy Commission.

Heilman, W. E., Liu, Y., Urbanski, S., Kovalev, V., & Mickler, R. (2014). Wildland fire emissions, carbon, and climate: Plume rise, atmospheric transport, and chemistry processes. *Forest Ecology and Management*, *317*, 70–79. https://doi.org/10.1016/j.foreco.2013.02.001

Hess, M., Koepke, P., & Schult, I. (1998). Optical properties of aerosols and clouds: The software package OPAC. *Bulletin of the American Meteorological Society*, *79*(5), 831–844. https://doi.org/10.1175/1520-0477(1998)079%3C0831:OPOAAC%3E2.0.CO;2

Hewitt, K. (1983). Place annihilation: Area bombing and the fate of urban places. *Annals of the Association of American Geographers*, *73*(2), 257–284. https://doi.org/10.1111/j.1467-8306.1983.tb01412.x

Holland, M. M., Bailey, D. A., Briegleb, B. P., Light, B., & Hunke, E. (2012). Improved sea ice shortwave radiation physics in CCSM4: The impact of melt ponds and aerosols on Arctic sea ice. *Journal of Climate*, *25*(5), 1413–1430. https://doi.org/10.1175/JCLI-D-11-00078.1

Huang, Y., Wu, S., Dubey, M. K., & French, N. H. F. (2013). Impact of aging mechanism on model simulated carbonaceous aerosols. *Atmospheric Chemistry and Physics*, *13*, 6329–6343. https://doi.org/10.5194/acp-13-6329-2013

Hunke, E. C., & Lipscomb, W. H. (2008), CICE: The Los Alamos sea ice model, documentation and software, version 4.0. Los Alamos National Laboratory tech. Rep. LA-CC-06-012, 76 p.

Hurrell, J. W., Holland, M. M., Gent, P. R., Ghan, S., Kay, J. E., Kushner, P. J., et al. (2013). The Community Earth System Model: A framework for collaborative research. *Bulletin of the American Meteorological Society*, *94*(9), 1339–1360. https://doi.org/10.1175/BAMS-D-12-00121.1

Kay, J. E., Deser, C., Phillips, A., Mai, A., Hannay, C., Strand, G., et al. (2015). The Community Earth System Model (CESM) large ensemble project: A community resource for studying climate change in the presence of internal climate variability. *Bulletin of the American Meteorological Society*, *96*(8), 1333–1349. https://doi.org/10.1175/BAMS-D-13-00255.1

Korycansky, D. G., Plesko, C. S., Jutzi, M., Asphaug, E., & Colaprete, A. (2009). Predictions for the LCROSS mission. *Meteoritics and Planetary Science*, *44*(4), 603–620. https://doi.org/10.1111/j.1945-5100.2009.tb00755.x

Lambe, A. T., Ahern, A. T., Wright, J. P., Croasdale, D. R., Davidovits, P., & Onasch, T. B. (2015). Oxidative aging and cloud condensation nuclei activation of laboratory combustion soot. *Journal of Aerosol Science*, *79*, 31–39. https://doi.org/10.1016/j.jaerosci.2014.10.001

Lawrence, D. M., Oleson, K. W., Flanner, M. G., Thornton, P. E., Swenson, S. C., Lawrence, P. J., et al. (2011). Parameterization improvements and functional and structural advances in Version 4 of Community Land Model. *Journal of Advances in Modeling Earth Systems*, *3*, 1–27 M03001.

Linn, R. R. (1997). A transport model for prediction of wildfire behavior. In *Los Alamos National Laboratory Science Report*, LA-13334-T, Los Alamos, NM: Los Alamos National Laboratory.

Linn, R. R., & Cunningham, P. (2005). Numerical simulations of grass fires using a coupled atmosphere–fire model: Basic fire behavior and dependence on wind speed. *Journal of Geophysical Research*, *110*, D13107. https://doi.org/10.1029/2004JD005597

Linn, R. R., Winterkamp, J., Colman, J. J., Edminster, C., & Bailey, J. D. (2005). Modeling interactions between fire and atmosphere in discrete element fuel beds. *International Journal of Wildland Fire*, *14*(1), 37–48. https://doi.org/10.1071/WF04043

Linn, R. R., Sieg, C. H., Koo, E., & Winterkamp, J. W. (2010). Using a physics-based model to characterize spotting potential for protection of the wildland urban interface, in *Final Report on JFSP 07–1–5-01, LA-UR-11-10587*. Los Alamos, NM.

Linn, R. R., Anderson, K., Winterkamp, J., Brooks, A., Wotton, M., Dupuy, J. L., et al. (2012). Incorporating field wind data into Firetec simulations of the International Crown Fire Modeling Experiment (ICFME): Preliminary lessons learned. *Canadian Journal of Forest Research-Revue Canadienne De Recherche Forestiere*, *42*(5), 879–898. https://doi.org/10.1139/x2012-038

Linn, R. R., Canfield, J. M., Cunningham, P., Edminster, C., Dupuy, J. L., & Pimont, F. (2012). Using periodic line fires to gain a new perspective on multi-dimensional aspects of forward fire spread. *Agricultural and Forest Meteorology*, *157*, 60–76. https://doi.org/10.1016/j.agrformet.2012.01.014

Margolin, L. G., & Reisner, J. M. (2016). Fully compressible solutions for early stage Richtmyer-Meshkov instability. *Computers and Fluids*, *151*, 46–57.

Marsh, D. R., Mills, M. J., Kinnison, D. E., Lamarque, J.-F., Calvo, N., & Polvani, L. M. (2013). Climate change from 1850 to 2005 simulated in CESM1(WACCM). *Journal of Climate*, *26*(19), 7372–7391. https://doi.org/10.1175/JCLI-D-12%2000558.1

Meinshausen, M., Smith, S. J., Daniel, J. S., Kainuma, M. L., Lamarque, J.-F., Matsmoto, K., et al. (2011). The RCP greenhouse gas concentrations and their extensions from 1765 to 2300. *Climatic Change*, *109*(1-2), 213–241. https://doi.org/10.1007/s10584-011-0156-z

Mills, M. J., Toon, O. B., Turco, R. P., Kinnison, D. E., & Garcia, R. R. (2008). Massive global ozone loss predicted following regional nuclear conflict. *Proceedings of the National Academy of Sciences of the United States of America*, *105*(14), 5307–5312. https://doi.org/10.1073/pnas.0710058105

Mills, M. J., Toon, O. B., Taylor, J. L., & Robock, A. (2014). Multidecadal global cooling and unprecedented ozone loss following a regional nuclear exchange. *Earth's Future*, *2*. https://doi.org/10.1002/2013EF00025, 161–176.

National Research Council (1985). *The Effects on the Atmosphere of a Major Nuclear Exchange* (p. 193). Washington, DC: National Academies Press.

Neale, R. B., Richter, J. H., Conley, A. J., Park, S., Lauritzen, P. H., Gettelman, A., & Williamson, D. L. (2010). Description of the NCAR Community Atmosphere Model (CAM 5.0), NCAR Tech, Note NCAR/TN-486+STR, Natl. Cent. For Atmos. Res., boulder, Colo.

Neale, R. B., Richter, J., Park, S., Lauritzen, P. H., Vavrus, S. J., Rasch, P. J., & Zhang, M. (2013). The mean climate of the Community Atmosphere Model (CAM4) in forced SST and fully coupled experiments. *Journal of Climate*, *26*(14), 5150–5168. https://doi.org/10.1175/JCLI-D-12-00236.1

Ogden, D. E., Glatzmaier, G. A., & Wohletz, K. H. (2008). Effects of vent overpressure on buoyant eruption columns: Implications for plume stability. *Earth and Planetary Science Letters*, *268*(3-4), 283–292. https://doi.org/10.1016/j.epsl.2008.01.014

Ogden, D. E., Wohletz, K. H., Glatzmaier, G. A., & Brodsky, E. E. (2008). Numerical simulations of volcanic jets: Importance of jet overpressure. *Journal of Geophysical Research*, *113*, B02204. https://doi.org/10.1029/2007JB005133

Oleson, K. W., Lawrence, D. M., Bonan, G. B., Flanner, M. G., Kluzek, E., Lawrence, P. J., et al. (2010). NCAR Tech. Note NCAR/TN-478+STR, Natl. Cent. for Atmos. Res., Boulder, Colo., doi:https://doi.org/10.5065/D6FB50WZ.

Pausata, F. S. R., Lindvall, J., Ekman, A. M. L., & Svensson, G. (2016). Climate effects of a hypothetical regional nuclear war: Sensitivity to emission duration and particle composition. *Earth's Future*, *4*(11), 498–511. https://doi.org/10.1002/2016EF000415

Penner, J. E., & Molenkamp, C. R. (1989). Predicting the consequences of nuclear war: Precipitation scavenging of smoke. *Aerosol Science and Technology*, *10*(1), 51–62. https://doi.org/10.1080/02786828908959220

Pimont, F., Dupey, J.-L., Linn, R. R., & Dupont, S. (2009). Validation of FIRETEC wind-flows over a canopy and fuel-break. *International Journal of Wildland Fire*, *18*, 775–790.

Pimont, F., Dupuy, J. L., Linn, R., Parsons, R., & Martin-StPaul, N. (2016). Wind-measurement accuracy in fire experiments: Lessons learned from large-eddy simulations in a homogeneous forest. *Agricultural and Forest Meteorology*, *232*, 479–488.

Pittock, A. B., Ackerman, T. P., Crutzen, P. J., MacCracken, M. C., Shapiro, C. S., & Turco, R. P. (1986). *Environmental Consequences of Nuclear War, SCOPE 28*, Volume I: Physical and Atmospheric Effects. (359 pp.; 2nd edition 1989). Chichester, UK: Wiley.

Reddington, C. L., McMeeking, G., Mann, G. W., Coe, H., Frontoso, M. G., Liu, D., et al. (2013). The mass and number size distributions of black carbon aerosol over Europe. *Atmospheric Chemistry and Physics*, *13*(9), 4917–4939. https://doi.org/10.5194/acp-13-4917-2013

Reid, J. S., Koppmann, R., Eck, T. F., & Eleuterio, D. P. (2005). A review of biomass emissions part II: Intensive physical properties of biomass burning particles. *Atmospheric Chemistry and Physics*, *5*(3), 799–825. https://doi.org/10.5194/acp-5-799-2005

Reisner, J. M., & Jeffery, C. A. (2009). A smooth cloud model. *Monthly Weather Review*, *137*(6), 1825–1843. https://doi.org/10.1175/2008MWR2576.1

Robock, A. (1989). Policy implications of nuclear winter and ideas for solutions. *Ambio*, *18*, 360–366.

Robock, A., & Toon, O. W. (2010). Local nuclear war, global suffering. *Scientific American*, *302*(1), 74–81. https://doi.org/10.1038/scientificamerican0110-74

Robock, A., Oman, L., Stenchikov, G. L., Toon, O. B., Bardeen, C., & Turco, R. P. (2007). Climatic consequences of regional nuclear conflicts. *Atmospheric Chemistry and Physics*, *7*(8), 2003–2012. https://doi.org/10.5194/acp-7-2003-2007

Robock, A., Oman, L., & Stenchikov, G. L. (2007). Nuclear winter revisited with a modern climate model and current nuclear arsenals: Still catastrophic consequences. *Journal of Geophysical Research*, *112*, D13107. https://doi.org/10.1029/2006JD008235

Ruxton, G. D. (2006). The unequal variance *t*-test is an underused alternative to Student's *t*-test and the Mann-Whitney *U* test. *Behavioral Ecology*, *17*(4), 688–690. https://doi.org/10.1093/beheco/ark016

Sakata, R., Grant, E. J., Furukawa, K., Misumi, M., Cullings, H., Ozasa, K., & Shore, R. E. (2014). Long-term effects of the rain exposure shortly after the atomic bombings in Hiroshima and Nagasaki. *Radiation Research*, *182*(6), 599–606. https://doi.org/10.1667/RR13822.1

Smith, R., Jones, P., Briegleb, B., Bryan, F., Danabasoglu, G., Dennis, J., et al. (2010). The Parallel Ocean Program (POP) reference manual, ocean component of the Community Climate System Model (CCSM). Los Alamos National Laboratory Tech. Rep. LAUR-10-01853, 141 p.

Stenke, A., Hoyle, C. R., Luo, B., Rozanov, E., Grobner, J., Maag, L., et al. (2013). Climate and chemistry effects of a regional scale nuclear conflict. *Atmospheric Chemistry and Physics*, *13*(19), 9713–9729. https://doi.org/10.5194/acp-13-9713

Taylor, K., Stouffer, R., & Meehl, G. (2012). An overview of CMIP5 and the experiment design. *Bulletin of the American Meteorological Society*, *93*(4), 485–498. https://doi.org/10.1175/BAMS-D-11-00094.1

Timmreck, C., Graf, H.-F., Lorenz, S. J., Niemeier, U., Zanchettin, D., Matei, D., et al. (2010). Aerosol size confines climate response to volcanic super-eruptions. *Journal of Geophysical Research*, *37*, L24705. https://doi.org/10.1029/2010GL045464

Toon, O. B., Turco, R. P., Robock, A., Bardeen, C., Oman, L., & Stenchikov, G. L. (2007). Atmospheric effects and societal consequences of regional scale nuclear conflicts and acts of individual nuclear terrorism. *Atmospheric Chemistry and Physics*, *7*(8), 1973–2002. https://doi.org/10.5194/acp-7-1973-2007

Toon, O. B., Robock, A., & Turco, R. P. (2008). Environmental consequences of nuclear war. *Physics Today*, *61*(12), 37–42. https://doi.org/10.1063/1.3047679

Turco, R. P., Toon, O. B., Ackerman, T. P., Pollack, J. B., & Sagan, C. (1983). Nuclear winter: Global consequences of multiple nuclear explosions. *Science*, *222*(4630), 1283–1292. https://doi.org/10.1126/science.222.4630.1283

Whittle, P. (1983). *Prediction and Regulation by Linear Least-Square Methods*. Minneapolis, MN: University of Minnesota Press. ISBN0–8166–1148-3

Wu, Y., Wang, X., Tao, J., Huang, R., Tian, P., Cao, J., et al. (2017). Size distribution and source of black carbon aerosol in urban Beijing during winter haze episodes. *Atmospheric Chemistry and Physics*, *17*(12), 7965–7975. https://doi.org/10.5194/acp-17-7965-2017

Zhang, R., Khalizov, A. F., Pagels, J., Zhang, D., Xue, H., & McMurry, P. H. (2008). Variability in morphology, hygroscopicity, and optical properties of soot aerosol during atmospheric processing. *Proceedings of the National Academy of Sciences*, *105*(30), 10,291–10,296. https://doi.org/10.1073/pnas.0804860105